Study of B meson decays with J/ψ and ϕ in the final states

A Dissertation
Presented to the Faculty of the Graduate School
of
the Graduate University for Advanced Studies
in Candidacy for the Degree of
Doctor of Philosophy

By
Yang Liu

Dissertation Director: Prof. Yoshihide Sakai
Co-adviser: Dr. Karim Trabelsi

September. 2008

Acknowledgments

I would like to thank my adviser, Prof. Yoshihide Sakai. His enormous physics knowledge and serious attitude on science give me a deep impression. His enthusiasm on the research sets an example for me. I also thank him for giving me a chance to stay in KEK to do my research on Belle physics. I would like to thank Dr. Karim Trabelsi, the co-adviser of my PhD research. He guided me through all the detailed analysis in my research.

Special thanks to Liming Zhang, a great partner of the research. He gave me a lot of help and encouragement. I thank Dr. Hideyuki Nakazawa, Dr. Yumi Uchida, Mr. Masaya Iwabuchi, Mr. Seng Zhang and Miss. Misa Miyai to give me a lot of help on Study and life when I stay at KEK.

I'd like to thank my parents for their sacrifice and support. Without the sacrifice, I will be only the body without spirit.

I'd like to thank all my friends for their support. Without you, the life is meaningless.

I thank every member of the Belle collaboration for their hard work to make the experiment run smoothly and successfully, to construct the detector and develop the software.

ABSTRACT

Study of B meson decays with J/ψ and ϕ in the final states

Yang Liu
the Graduate University for Advanced Studies
September. 2008

We study the decay modes of B meson decay to final states including J/ψ and ϕ mesons based on a large amount of data sample at the $\Upsilon(4S)$ state collected with Belle detector in KEKB asymmetric energy e^+e^- collider.

The decay $B^0 \to J/\psi\phi$ is expected to involve W-exchange and final state interaction (FSI) processes. The mechanisms contributing to this decay can be divided into four categories: 1) The photo-production; 2) The tri-gluon fusion; 3) The rescattering effect; 4) The ω - ϕ mixing. The dominant contribution is from ω - ϕ mixing and the branching fraction for this decay is estimated to be $(1.8 \pm 0.3) \times 10^{-7}$.

We perform a search for $B^0 \to J/\psi\phi$ decays using a data sample of 605 fb^{-1} containing 657×10^6 $B\bar{B}$ pairs.

We reconstruct B mesons from the decays $J/\psi \to \ell^+\ell^-$ ($\ell = e, \mu$) and $\phi \to K^+K^-$. Events are required to pass a basic hadronic event selection. We identify B candidates using two widely used kinematic variables calculated in the center-of-mass system:the beam-energy constrained mass ($M_{\rm bc} \equiv \sqrt{E^2_{\rm beam} - P^2_B}$) and the energy difference ($\Delta E \equiv E_B - E_{\rm beam}$), where $E_{\rm beam}$ is the beam energy, P_B and E_B are the reconstructed momentum and energy of the B^0 candidate. We select B candidates within the range -0.2 GeV $< \Delta E < 0.3$ GeV and 5.27 GeV/c^2 $< M_{\rm bc} <$ 5.29 GeV/c^2 for final analysis.

We study reconstruction efficiency and event selection criteria using a large signal Monte Carlo (MC) sample. To study the background, we use a MC sample corresponding to 3.86×10^6 generic $B\bar{B}$ decays (59 times that of real data) that includes all known $B \to J/\psi X$ processes as well as sideband region.

The dominant background comes from $B\bar{B}$ events with B decays to J/ψ. We find that the dominant backgrounds come from $B^0 \to J/\psi K^{*0}(892)[\to K^-\pi^+]$ and $B^{0/-} \to J/\psi K_1(1270)[\to K^-\pi^+\pi^{0/-}]$. In both cases, a pion is misidentified as a kaon, and in the latter case, the other pion is missed. The former has a peak at $\Delta E \sim 0.1 \sim$ GeV, while the latter has a broad peak in the negative ΔE region. The remaining background is due to random combinations of J/ψ and ϕ candidates and does not have structure in the ΔE distribution (referred to as combinatorial background).

The signal yield is extracted by performing an unbinned extended maximum-likelihood fit to the ΔE distribution of candidate events. The signal PDF is modeled by a sum of two Gaussians. The background PDFs are two Gaussians for the $J/\psi K_1$ component, a bifurcated Gaussian for the $J/\psi K^{*0}$ component and a second-order polynomial for combinatorial background, respectively. The parameters of these PDFs are determined from MC simulations.

We obtain a signal yield of $4.6\ ^{+3.1}_{-2.5}$ events with a statistical significance of 2.3σ. As no significant signal is found for the $B^0 \to J/\psi\phi$ decay mode, we derive an upper limit on the yield at the 90% confidence level by a frequentist method using ensembles of pseudo-experiments. Finally an upper limit at the 90% confidence level is obtained:

$$\mathcal{B}(B^0 \to J/\psi\phi) < 9.4 \times\ 10^{-7}. \tag{1}$$

This result improves upon the previous result by about a factor of 10 and is consistent with the theory prediction. The result shows that a large enhancement from rescattering is not likely in this decay mode. To check the prediction more precisely, a larger data sample is needed.

Contents

List of Figures

List of Tables

Chapter 1

Introduction

This thesis describes the measurement of branching ratio of $B \to J/\psi\phi$. We discuss the possible mechanisms that contribute to this decay mode in chapter 1; we give a brief introduction to KEKE collider and Belle detector in chapter 2; in chapter 3, we describe the analysis method; in chapter 4, we give a full description on the analysis process and provide the results; in the last chapter, we give the conclusion.

1.1 Standard Model

In the twentieth century, human being has made great achievements in the understanding of the universe. From the dominating Newtonian mechanics and Maxwellian electrodynamics before the twentieth century to modern theory framework known as the Standard Model (SM) [1] which is a $SU(3) \otimes SU(2) \otimes U(1)$ gauge theory, the fundamental electroweak and strong interactions have been well described. According to this model, all matter is built from a small number of fundamental spin 1/2 particles, or fermions: six quarks and six leptons.

Tab. 1.1 and Tab. 1.2 give the symbol, mass, the ratio of its electric charge Q to the elementary charge e of the electron and the Spin-parity of each of the various fundametal constituents.

In the SM, there are four types of fundamental interaction: Strong interaction, Electromagnetic interaction, Weak interaction and Gravitational interaction. The

Quarks	Symbol	Mass MeV/c^2	Electric Charge Q/e	Spin-parity J^P
Up	u	~ 3	$+\frac{2}{3}$	$\frac{1}{2}^+$
Down	d	~ 5	$-\frac{1}{3}$	$\frac{1}{2}^+$
Charm	c	~ 1250	$+\frac{2}{3}$	$\frac{1}{2}^+$
Strange	s	~ 95	$-\frac{1}{3}$	$\frac{1}{2}^+$
Top	t	~ 174200	$+\frac{2}{3}$	$\frac{1}{2}^+$
Bottom	b	~ 4500	$-\frac{1}{3}$	$\frac{1}{2}^+$

Table 1.1: The quarks

Leptons	Symbol	Mass MeV/c^2	Electric Charge Q/e	Spin J^P
Electron	e	~ 511	-1	$\frac{1}{2}$
Muon	μ	~ 106	-1	$\frac{1}{2}$
Tau	τ	~ 1777	-1	$\frac{1}{2}$
Electron nertrino	ν_e	<0.000002	0	$\frac{1}{2}$
Muon neutrino	ν_μ	<0.19	0	$\frac{1}{2}$
Tau neutrino	nu_τ	<18	0	$\frac{1}{2}$

Table 1.2: The leptons

different interactions are described in quantum language in terms of the exchange of boson mediators between the fermion constituents. These boson mediators are listed in Tab. 1.3.

The theory about the particles and the interactions in the SM includes two parts: the electroweak theory describing the unification of the electromagnetic and weak forces and the quantum chromodynamics (QCD) describing the strong interaction.

To date, the SM has been tested by huge number of experiments to a high degree of precision, and is viewed as a reliable and successful theory in particle interactions. In the new century, physics phenomena predicted by the SM but not yet observed is one of the main objectives of high energy physics.

Although SM has achieved great success, it is an uncomplete theory. It does not

Name	Interaction	Relative Magnitudes	Spin-parity
Gluon, g	Strong	1	1^-
Photon, γ	Electromagnetic	10^{-2}	1^-
$W^{\pm}, Z^0$	Weak	10^{-7}	$1^-, 1^+$
Graviton,	Gravity	10^{-39}	2^+

Table 1.3: The boson mediators

attempt to explain gravity and it has too many unrelated parameters. The search for New Physics never stops drawing great attention of the physicists around the world.

1.2 CKM Matrix

In the SM, quarks and leptons are assigned to be left-handed doublets and right-handed singlets. The SU(2) quark doublets of weak isospin is referred as

$$\begin{array}{l}\text{charge} = +\frac{2}{3}e \\ \text{charge} = -\frac{1}{3}e\end{array} \underbrace{\begin{pmatrix} u \\ d \end{pmatrix}\begin{pmatrix} c \\ s \end{pmatrix}\begin{pmatrix} t \\ b \end{pmatrix}}_{\text{quarks}}, \tag{1.1}$$

where the flavors are assigned by the strong interaction.

In the weak interactions, quark flavor can change by transition to different charge quark with emission or absorption of a $W^{\pm}$ boson, which is also called the propagator. With the notation $u_i (i = 1, 2, 3)$ to represent the spinor $u,\ c,\ t$ and $d_j (j = 1, 2, 3)$ to denote $d,\ s,\ b$, the physical dynamics within doublets can be described by a Lagrangian term [2]

$$\mathcal{L}_W = -\frac{g}{\sqrt{2}}\left(W^+_\mu \bar{u}_i \gamma^\mu \frac{1-\gamma_5}{2} V_{ij} d_j + W^-_\mu \bar{d}_j \gamma^\mu \frac{1-\gamma_5}{2} V^*_{ij} u_i\right) , \tag{1.2}$$

where $W^{\pm}$ is the W gauge boson field and V is a unitary matrix which relates strong and weak quark eigenstates. The nature is complicated through the V known as the Cabibbo-Kobayashi-Maskawa (CKM) [3] flavor mixing matrix, which has non-zero off-diagonals. By convention, the CKM matrix is expressed as a 3×3 matrix operating on $d,\ s,\ b$:

$$\begin{pmatrix} V_{ud} & V_{us} & V_{ub} \\ V_{cd} & V_{cs} & V_{cb} \\ V_{td} & V_{ts} & V_{tb} \end{pmatrix} \begin{pmatrix} d \\ s \\ b \end{pmatrix} \tag{1.3}$$

In general, each of the 9 elements of the 3×3 matrix V in Eqn. 1.3 is a complex number, so 18 parameters are needed to fully describe V. However, the unitary requirements $V^\dagger V = \mathbf{I}$ provides 9 constraints. Moreover, two arbitrary relative phases in the rows with another two in columns and one arbitrary overall phase eliminates 5 more free parameters. Thereby 4 independent parameters is used to express the CKM matrix. The Wolfenstein parameterization [4] of the CKM matrix is most commonly used, where $V_{us} \equiv \lambda$, the sine of the Cabibbo angle. Now the matrix can be expanded

as

$$\mathbf{V} = \begin{pmatrix} 1-\frac{1}{2}\lambda^2 & \lambda & A\lambda^3(\rho - i\eta) \\ -\lambda & 1-\frac{1}{2}\lambda^2 & A\lambda^2 \\ A\lambda^3(1-\rho-i\eta) & -A\lambda^2 & 1 \end{pmatrix} + \mathcal{O}(\lambda^4)\ . \tag{1.4}$$

with A,ρ and η being real parameters of order unity.

Among the four parameters, λ and A are relatively well known from corresponding semi-leptonic decays: $|V_{us}| = 0.2257 \pm 0.0021$ from K_L decays and $|V_{cb}| = (41.6 \pm 0.6) \times 10^{-3}$ from inclusive and exclusive $b \to cl\bar{\nu}_l$ decays [13]. The determination of the other two parameters ρ and η is conveniently depicted as a contour in plane of (ρ, η). It corresponds to the unitarity relation of the CKM matrix applied to the first and third columns:

$$V_{ud}V_{ub}^* + V_{cd}V_{cb}^* + V_{td}V_{tb}^* = 0 \tag{1.5}$$

This relation may be presented in the complex plane as in Fig. 1.1, which is called the "unitarity triangle". The three angles of the unitarity triangle represent the complex phase of the combinations:

$$\phi_1 = \arg[-\frac{V_{cd}V_{cb}^*}{V_{td}V_{tb}^*}], \phi_2 = \arg[-\frac{V_{td}V_{tb}^*}{V_{ud}V_{ub}^*}], \phi_3 = \arg[-\frac{V_{ud}V_{ub}^*}{V_{cd}V_{cb}^*}]. \tag{1.6}$$

The unitarity triangle is also can be shown in (ρ, η) plane as Fig. 1.2. Its vertices are exactly (0,0), (1,0) and $(\bar{\rho}, \overline{\eta})$, where

$$\bar{\rho} = \rho(1 - \lambda^2/2), \bar{\eta} = \eta(1 - \lambda^2/2) \tag{1.7}$$

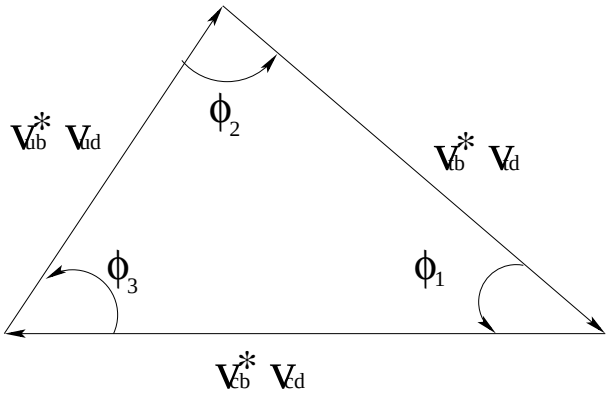

Figure 1.1: Unitarity triangle

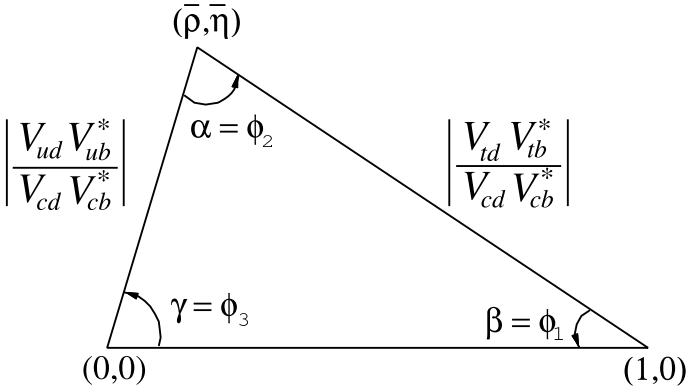

Figure 1.2: Unitarity triangle in $\overline{\rho} - \overline{\eta}$ plane.

1.3 Physics in $B^0 \to J/\psi\phi$

Since the quarks involved in the final states of $B^0 \to J/\psi\phi$ decay are all different from the initial quarks, the decay diagrams in the lowest order of weak interaction have to involve W-exchange or hadronic final state interactions. Therefore, the branching fraction is expected to be much suppressed compared to other B decays involving J/ψ, such as $B \to J/\psi K^*$ and $J/\psi\pi(\rho)$ decays.

The mechanisms that contribute to its decay amplitude can be catalogued into four classes: 1) The ϕ meson is produced through tri-gluon fusion (due to Landau-Yang theorem [5]) which is formally the reason why this channel is suppressed by Okubo-Zweig-Iizuka (OZI) rule [6]; 2) The ϕ meson is produced through photo emission; 3) $J/\psi\phi$ are produced through long-distance final state interaction (rescattering), for instance $\bar{B}^0 \to D_s^{*+} D_s^{*-} \to J/\psi\phi$; 4) ϕ is produced through $\omega - \phi$ mixing. The quark diagrams contributing to this decay mode are shown in Fig. 1.3.

1.3.1 Photo-production

Fig. 1.3(b) shows the diagram for photo-production. $B^0 \to J/\psi\phi$ can be regarded as a cascade process $B^0 \to J/\psi\gamma \to J/\psi\phi$. Thus, basically we can reproduce the photo-production by studying $B \to V\gamma$ which has been well studied in the framework of Soft Collinear Effective Theory (SCET) [7].

We can start the calculation from the rough estimation.

$$\begin{aligned} \mathcal{B}(B^0 \to J/\psi\phi) &\simeq R_\phi \mathcal{B}(B^0 \to J/\psi\gamma) \\ R_\phi &= \left| -\frac{1}{3} e \frac{f_\phi m_\phi}{m_\phi^2} \right|^2 \simeq 0.0003\,, \end{aligned} \tag{1.8}$$

where f_ϕ and m_ϕ are the decay constant and mass of ϕ meson respectively. Eqn. 1.8 is derived as following. The decay amplitude of $B^0 \to J/\psi\gamma$ is written as $\mathcal{A}^\mu \epsilon_\mu^*(\gamma)$, then the decay amplitude of $B^0 \to J/\psi\phi$ through photo-production is

$$\begin{aligned} & \mathcal{A}_{\text{p.p.}}(B^0 \to J/\psi\phi) \simeq \mathcal{A}^\mu(B^0 \to J/\psi\gamma) \frac{-i g_{\mu\nu}}{q^2} \left(-i \frac{1}{3} e \right) \langle \phi | \bar{s} \gamma^\nu s | 0 \rangle \\ = \;& \mathcal{A}(B^0 \to J/\psi\gamma) \frac{1}{m_\phi^2} \left(i \frac{1}{3} e f_\phi m_\phi \right), \end{aligned} \tag{1.9}$$

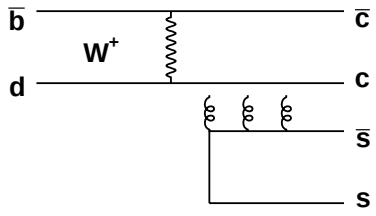

(a) tri-gluon fusion

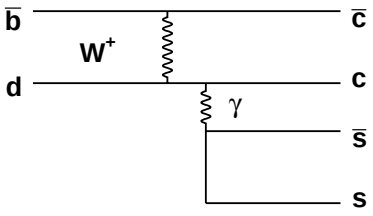

(b) photo-production

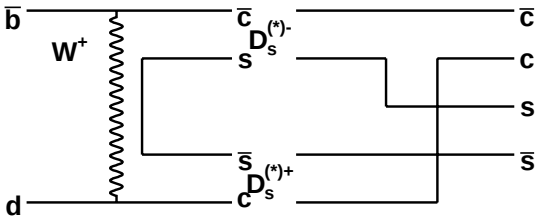

(c) final state interaction (OZI allowed rescattering)

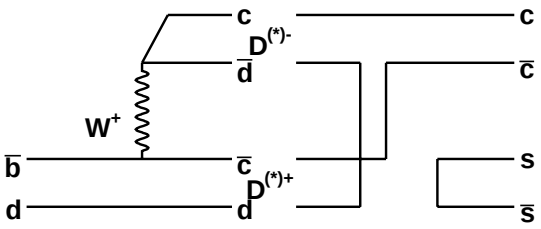

(d) final state interaction (OZI suppressed rescattering)

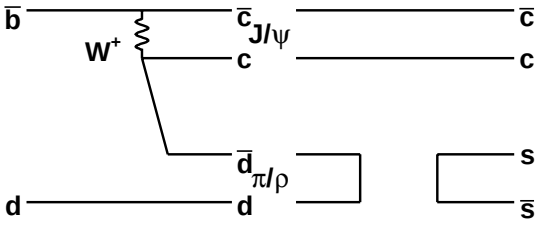

(e) final state interaction (OZI and color suppressed rescattering)

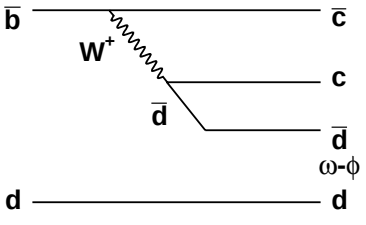

(f) $\omega - \phi$ mixing

Figure 1.3: The feynman diagrams contributing to the decay of $B \to J/\psi\phi$.

where we use

$$\langle \phi | \bar{s} \gamma_\mu s | 0 \rangle = -i f_\phi m_\phi \epsilon^*_\mu(\phi) \,, \tag{1.10}$$

with ϕ meson polarization vector $\epsilon^*_\mu(\phi) = \epsilon^*_\mu(\gamma)$ and decay constant $f_\phi \simeq 0.221 \pm 0.003$ GeV which can be extracted from the decay width $\phi \to \ell^+\ell^-$. Y.D.Yang et al have shown that $\mathcal{B}(B^0 \to J/\psi\gamma) < 10^{-7}$ in a naive factorization and a QCD factorization.[8]. The photo-production leads to a very small branching ratio for $B^0 \to J/\psi\phi$ to be less than 10^{-11}. The photo-production process $B^0 \to \phi\gamma \to J/\psi\phi$ can be also considered. The $\mathcal{B}(B^0 \to \phi\gamma)$ is estimated to be 3.6×10^{-12} using QCD factorization formalism [9] and the contribution to $B^0 \to J/\psi\phi$ is smaller than $B^0 \to J/\psi\gamma \to J/\psi\phi$.

1.3.2 Tri-gluon Fusion Process

Fig. 1.3(a) shows the diagram for tri-gluon fusion process. It is a W-bosen exchange process with an $s\bar{s}$ pair is attached through three gluons. Due to the complicated QCD dynamics, it is hard to calculate the tri-gluon fusion reliably. Roughly, the tri-gluon fusion contribution is order of $\alpha_s^3 \sim 0.3^3 \sim 0.03$. Thus, naively comparing to the photo-production with the order of $\alpha_{\rm em} \sim 0.01$ (in amplitude), the branching fraction of the tri-gluon fusion process is about 10 times larger than the photo-production process, *i.e.* $\leq 10^{-10}$.

1.3.3 Rescattering Effect

As shown in Fig. 1.3(c)-Fig. 1.3(e), there are several possible rescattering processes which lead to $B^0 \to J/\psi\phi$ decay. The $B^0 \to D_s^{(*)+} D_s^{(*)-} \to J/\psi\phi$ (Fig. 1.3(c)) proceeds via W-exchange diagram for intermediate states and OZI-allowed rescattering. While, $B^0 \to D^{(*)+} D^{(*)-} \to J/\psi\phi$ (Fig. 1.3(d)) proceeds via tree diagram for intermediate states and OZI-suppressed rescattering. The $B^0 \to J/\psi\pi(\eta,\rho) \to J/\psi\phi$ (Fig. 1.3(e)) is further color-suppressed for intermediate states compared with the process in Fig. 1.3(d).

The branching fractions for $B^0 \to D_s^{(*)+} D_s^{(*)-}$ have not been measured yet. The theoretical calculations give $(2-3) \times 10^{-4}$ based on heavy-light chiral perturbation theory [10] and $(6-9) \times 10^{-5}$ based on pQCD model [11]. However, recent Belle result, $\mathcal{B}(B^0 \to D_s^+ D_s^-) < 3.6 \times 10^{-5}$ [12], implies that W-exchange amplitudes may be further suppressed. Phenomenologically, the branching fraction for $B^0 \to D_s^{(*)+} D_s^{(*)-}$ can be estimated from the $B^0 \to D_s^- K^+$ decay which also proceeds via W-exchange diagram (see Fig. 1.4(a)) with branching fraction of $(3.1 \pm 0.8) \times 10^{-5}$ [13]. Taking account the differences of meson wave functions (K^+ and D_s^+) and the CKM factors (V_{ud} and V_{cd}), $\mathcal{B}(B^0 \to D_s^+ D_s^-) \sim 0.16 \times \mathcal{B}(B^0 \to D_s^- K^+) \sim 5 \times 10^{-6}$ is estimated [14]. Another approach taking the ratio of W-exchange and tree diagrams from $\mathcal{B}(B^0 \to D_s^- K^+)/\mathcal{B}(B^0 \to D^- \pi^+) \sim 0.01$ gives a similar estimation $\mathcal{B}(B^0 \to D_s^+ D_s^-) \sim 0.01 \times \mathcal{B}(B^+ \to D^+ D^0) \sim 4 \times 10^{-6}$ [15].

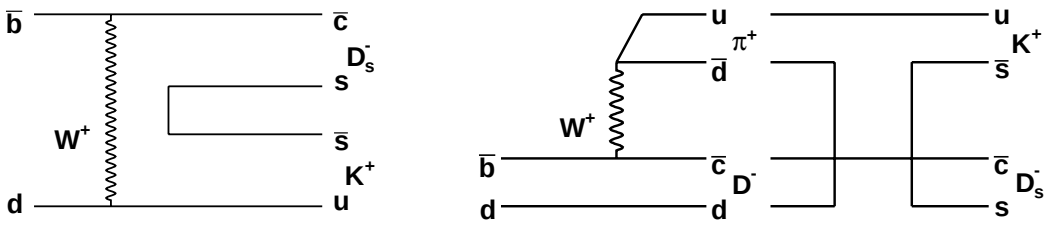

(a) W-exchange

(b) $B^0 \to D^- \pi^+$ and rescattering to $D_s^- K^+$. (OZI allowed)

Figure 1.4: The feynman diagrams contributing to the decay of $B \to D_s^- K^+$.

The $B^0 \to D_s^- K^+$ can be also used to estimate the suppression factor of the rescattering process. The (OZI-allowed) rescattering from $B^0 \to D^- \pi^+$ can also contributes to $B^0 \to D_s^- K^+$ as shown in Fig. 1.4(b). The ratio of branching fractions of these two decays indicates the contribution of the rescattering process is at most same level as W-exchange contribution and $\sim 1/100$ of intermediate process (assuming these two amplitudes do not have strong destructive interference).

Based on above discussions, the branching fraction for $B^0 \to D_s^{(*)+} D_s^{(*)-} \to J/\psi\phi$ is estimated to be $O(10^{-8})$.

The branching fraction of $B^0 \to D^{(*)+} D^{(*)-}$ is about two orders of magnitude larger than that of $B^0 \to D_s^{(*)+} D_s^{(*)-}$, while rescattering process is OZI-suppressed. It is difficult to estimate the OZI-suppression, but it is expected to be well below $O(10^{-1})$ in amplitude (i.e. $O(10^{-2})$ in branching fraction) as discussed in Sec.1.3.2. Therefore, contribution of Fig. 1.3(d) is expected to be smaller than that of Fig. 1.3(c). The contribution of Fig. 1.3(e) is further suppressed.

1.3.4 $\omega - \phi$ Mixing

The mixing between the vector mesons ω and ϕ plays an important role in the understanding of SU(3) breaking in QCD. In QCD, this mixing is entirely generated by the light quark mass differences. In addition, QED effects by photon exchange lead to a further mixing contribution.

The ω and ϕ mesons are a mixture of the SU(3) siglet ω_0 and the octet ω_8 states,

$$\phi = \cos\theta_V \omega_8 - \sin\theta_V \omega_0, \tag{1.11}$$

$$\omega = \sin\theta_V \omega_8 + \cos\theta_V \omega_0, \tag{1.12}$$

where

$$\omega_8 = (u\bar{u} + d\bar{d} - 2s\bar{s})/\sqrt{6}, \tag{1.13}$$

$$\omega_0 = (u\bar{u} + d\bar{d} + s\bar{s})/\sqrt{3}. \tag{1.14}$$

The ϕ and ω wave functions are then given by

$$\phi = (u\bar{u} + d\bar{d})(\frac{1}{\sqrt{6}}\cos\theta_V - \frac{1}{\sqrt{3}}\sin\theta_V) - s\bar{s}(\frac{2}{\sqrt{6}}\cos\theta_V + \frac{1}{\sqrt{3}}\sin\theta_V), \tag{1.15}$$

$$\omega = (u\bar{u} + d\bar{d})(\frac{1}{\sqrt{6}}\sin\theta_V + \frac{1}{\sqrt{3}}\cos\theta_V) + s\bar{s}(-\frac{2}{\sqrt{6}}\sin\theta_V + \frac{1}{\sqrt{3}}\cos\theta_V), \tag{1.16}$$

The stict OZI limit corresponds to the ideal mixing angle θ_I

$$\tan\theta_I = \frac{1}{\sqrt{2}} \rightarrow \theta_I = 35.3^\circ, \tag{1.17}$$

and the ideal ϕ and ω states are

$$\omega^{ideal} = 2\omega_0/\sqrt{6} + \omega_8/\sqrt{3} = (u\bar{u} + d\bar{d})/\sqrt{2}, \tag{1.18}$$

$$\phi^{ideal} = \omega_0/\sqrt{3} - 2\omega_8/\sqrt{6} = s\bar{s}, \tag{1.19}$$

It is further instructive to rewrite the ϕ and ω wave functions as follows

$$\phi = -\sin\delta\omega^{ideal} + \cos\delta\phi^{ideal}, \tag{1.20}$$

$$\omega = \cos\delta\omega^{ideal} + \sin\delta\phi^{ideal}, \tag{1.21}$$

where $\delta = \theta_V - \theta_I$. The physical mixing angle θ_V can be determined from the masses of the mesons in the vector meson nonet and differs from the ideal mixing angle. Using the quadratic Gell-Mann-Okubo mass formula, the physical mixing angle of the vector mesons can be obtained as $\theta_V = 39^\circ$. A simplified analysis[17] implies a mixing angle of $\delta = -(3.34 \pm 0.17)^\circ$, while the most recent treatment[18] implies an energy–dependent mixing which varies from -0.45° at the ω mass to -4.64° at the ϕ mass.

Neglecting small phase space differences between processes with ϕ or ω in the final states, Eq. 1.20 and Eq. 1.21 imply [19]:

$$\mathcal{B}(B^0 \rightarrow J/\psi\phi) = \tan^2\delta\mathcal{B}(B^0 \rightarrow J/\psi\omega). \tag{1.22}$$

The $\mathcal{B}(B^0 \rightarrow J/\psi\omega)$ has not been measured yet, but $\mathcal{B}(B \rightarrow J/\psi\rho^0) = (2.7 \pm 0.4) \times 10^{-5}$ [20] can be used as an approximation. The approximately equal decay rates measured for $\mathcal{B}(B^0 \rightarrow \bar{D}^0\rho^0) = (2.9 \pm 1.1) \times 10^{-4}$ and $\mathcal{B}(B^0 \rightarrow \bar{D}^0\omega) = (2.5 \pm 0.6) \times 10^{-4}$ [13]confirm this assumption. Using Eq. 1.22 with a universal value of $\delta = 4.64^\circ$, we can give a evaluation of $\mathcal{B}(B \rightarrow J/\psi\phi) = (1.8 \pm 0.3) \times 10^{-7}$.

1.3.5 Summary of $Br(B^0 \to J/\psi\phi)$ Estimation

We have discussed the four mechanisms that contribute to the decay mode $B \to J/\psi\phi$ and give the estimations of the branching fraction of each mechanism. We find that the dominant contribution is from $\omega - \phi$ mixing which is at the order of 10^{-7}.

The contribution of the rescattering process from $B^0 \to D_s^{(*)+} D_s^{(*)-}$ is estimated to be the order of 10^{-8}. Howerver, it should be noted that the estimation has large uncertainty. The $\mathcal{B}(B^0 \to D_s^+ D_s^-)$ may be close to the current experimental upper limit (a few $\times 10^{-5}$) or $\mathcal{B}(B^0 \to D_s^{*+} D_s^{*-})$ may be larger since current experimental limits are $\sim 10^{-4}$. Also, the rescattering effect may be much larger than that of $B^0 \to D^- \pi^+ \to D_s^- K^+$ case (for example, only $\sim \lambda$ suppression in amplitude). Then, the rescattering contribution can be $> 10^{-6}$.

The photo-production and tri-gluon fusion process gives much smaller and negligible contributions.

Previously, the BaBar collaboration searched for this decay mode and set an upper limit $\mathcal{B} < 9.2 \times 10^{-6}$ at the 90 % confidence level based on $56 \times 10^6 B\bar{B}$ pairs [21]. This upper limit is much larger than above estimations.

Chapter 2

Experimental Apparatus

This analysis is based on data accumulated by the Belle detector at the B factory KEKB. The experiment is located at the High Energy Accelerator Research Organization (KEK) in Japan. Its main physics goal is to study the origin of CP violation in B decays. The experiment was started in 1999 and has achieved many physics results until now. In this chapter, we will give a brief introduction to the KEKB collider and the Belle detector.

2.1 The KEKB Accelerator

The KEKB is an energy-asymmetric e^+e^- collider running mainly at the $\Upsilon(4S)$ resonance, $\sqrt{s} = 10.58$ GeV. Currently it has the highest luminosity in the world. Fig. 2.1 shows the history of integrated luminosity of the KEKB.

The KEKB accelerator [22] has two rings: a low-energy ring (LER) for positrons and a high-energy ring (HER) for electrons. Both rings are located in the already existing TRISTAN tunnel with a circumference of 3 km. The beam energies are 3.5 GeV for e^+ and 8.0 GeV for e^-. The center-of-mass (CM) energy is 10.580 GeV, corresponding to the $\Upsilon(4S)$ resonance, which is just above the $B\overline{B}$ production threshold. The $e^+e^- \to \Upsilon(4S)$ cross section is about 1.1 nb. At the same energy, the $e^+e^- \to q\bar{q}$ ($q = u, d, s,$ or c) continuum process has a cross section of 3.7 nb, with $c\bar{c} \sim 1.30$ nb. In addition, KEKB sometimes runs at an energy 60 MeV below the

resonance to measure the continuum process and at the energy of $\Upsilon(1S)$, $\Upsilon(3S)$, $\Upsilon(5S)$ states. Figure. 2.2 shows the total e^+e^- annihilation cross section as a function of the CM energy in the region of the Υ resonances. The configuration of KEKB factory is shown in Fig.2.3.

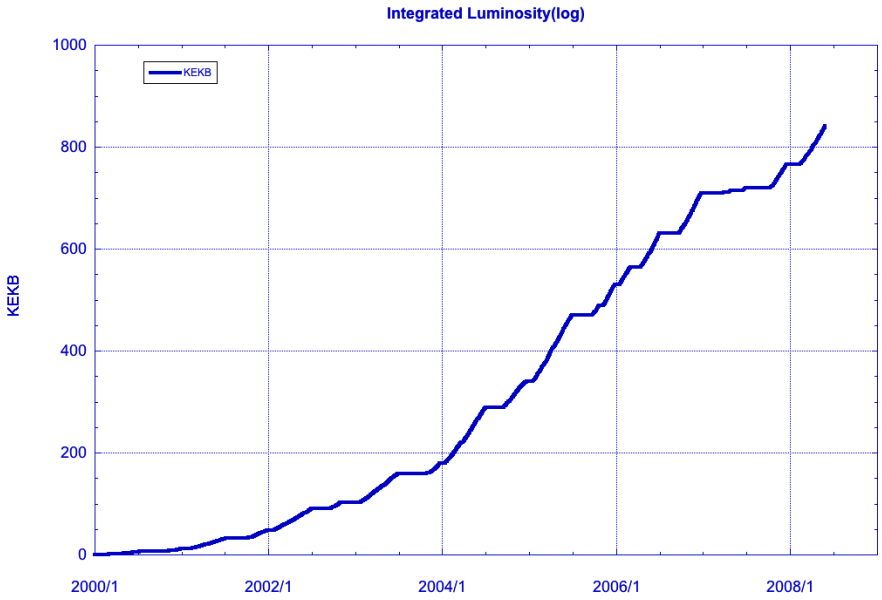

Figure 2.1: Total integrated luminosity of KEKB (till Jun, 2008)

The different energies of electron and positron beams give to the two B mesons produced from $\Upsilon(4S)$ a boost in the beam direction. The Lorentz boost factor $\beta\gamma$=0.425 corresponds to about 200 μm distance of the two B meson decay vertices, which allows us to study the time evolution of B mesons via their decay vertices.

In order to reduce parasitic collisions near the interaction region, KEKB has a unique design with $\pm$11 mrad crossing angle (See Fig. 2.4) of the e^+e^- beams instead of bending magnets. This feature provides the possibility to obtain higher peak luminosities. The KEKB was designed to operate with a peak luminosity of 10^{34} cm^{-2}s^{-1}, which corresponds to 100 fb^{-1} integrated luminosity, or $\sim 10^8$ $B\overline{B}$ pairs per year. KEKB has achieved a peak luminosity of 1.71×10^{34} cm^{-2}s^{-1}. Till now, the integrated luminosity of KEKB has exceeded 850 fb^{-1}.

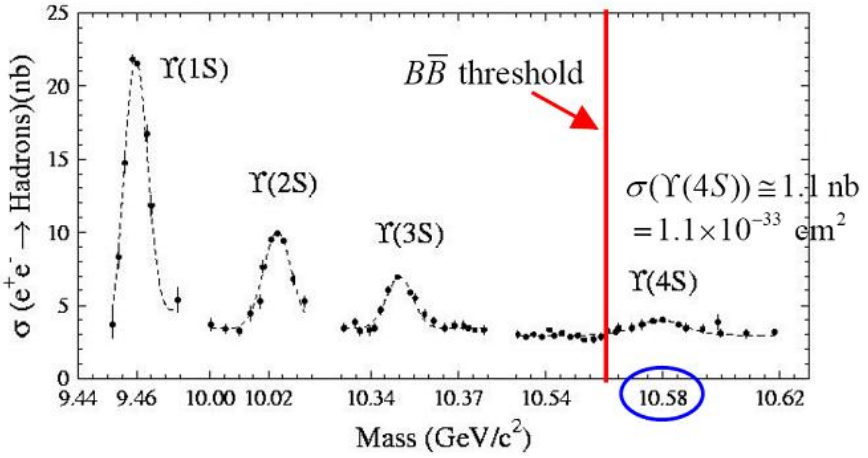

Figure 2.2: The cross-section for the annihilation process $e^+e^- \rightarrow$ hadrons, as a function of center-of-mass energy.

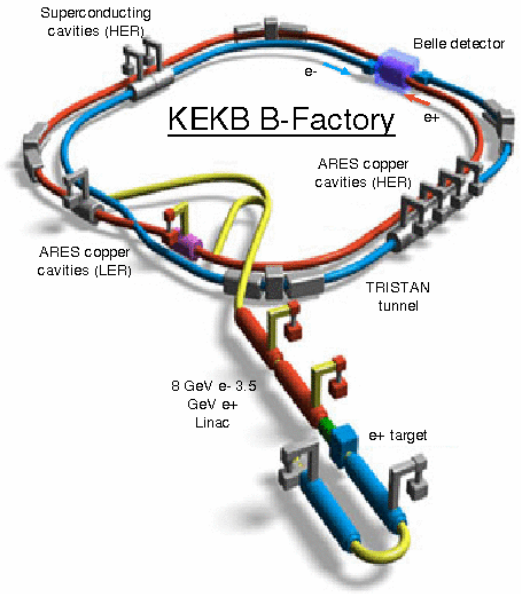

Figure 2.3: A graphical illustration of the KEKB accelerator.

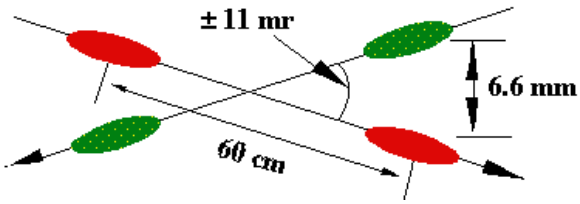

Figure 2.4: The finite angle beam crossing scheme.

2.2 Belle Detector

The Belle detector [23] is a large-solid-angle magnetic spectrometer that consists of a silicon vertex detector (SVD), a central drift chamber (CDC), an array of aerogel threshold Cherenkov counters (ACC), a barrel-like arrangement of time-of-flight scintillation counters (TOF), and a electromagnetic calorimeter (ECL) comprised of CSI(Tl) crystals located inside a superconducting solenoid coil that provides a 1.5 T magnetic field. An iron flux-return located outside the coil is instrumented to detect K_L^0 mesons and to identify muons (KLM). Two inner detector configurations were used. A 3-layer SVD with a 2 cm radius beampipe was used until 2003 (SVD1). A 1.5 cm radius beampipe, a 4-layer SVD, and a small-cell inner drift chamber were then installed (SVD2). The configuration of the Belle detector is shown in Fig. 2.5 and Fig. 2.6. Performance parameters of each sub-detector are summarized in Table. 2.1.

2.2.1 Beam Pipe and SVD

The precise determination of decay vertices is an essential requirement of the Belle experiment. In order to reach this goal, the vertex detector should be placed as close to the interaction point (IP) as possible, and a thin beam pipe is preferred.

The originally designed beam pipe has an inner radius of 2.0 cm, and an outer wall 2.3 cm in radius. Fig. 2.7 shows the cross section of the beam pipe at the interaction point. The central part (-4.6 cm$\leq z \leq$10.1 cm) of the beam pipe is a double-wall beryllium cylinder with 0.5 mm thickness. A 2.5 mm gap between the inner and outer walls of the cylinder contains helium gas for cooling. The material in the beam pipe is minimized to reduce multiple Coulomb scattering, and the total thickness of the

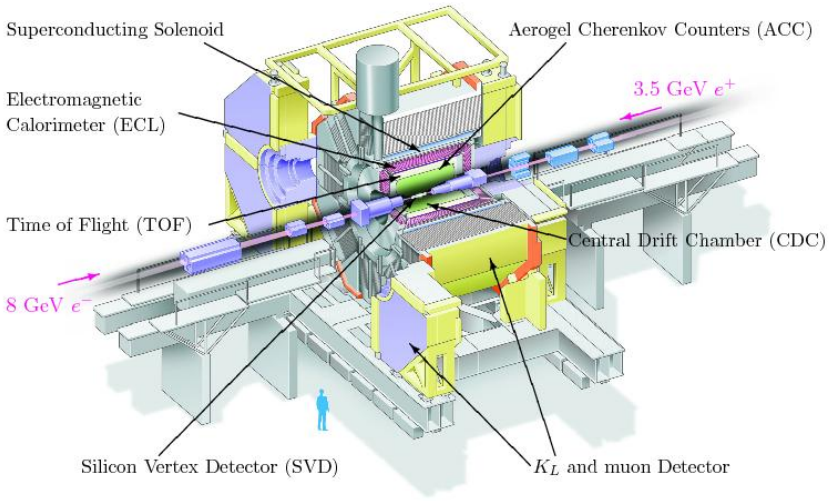

Figure 2.5: A graphical illustration of the Belle detector. The position of each sub-detector is indicated.

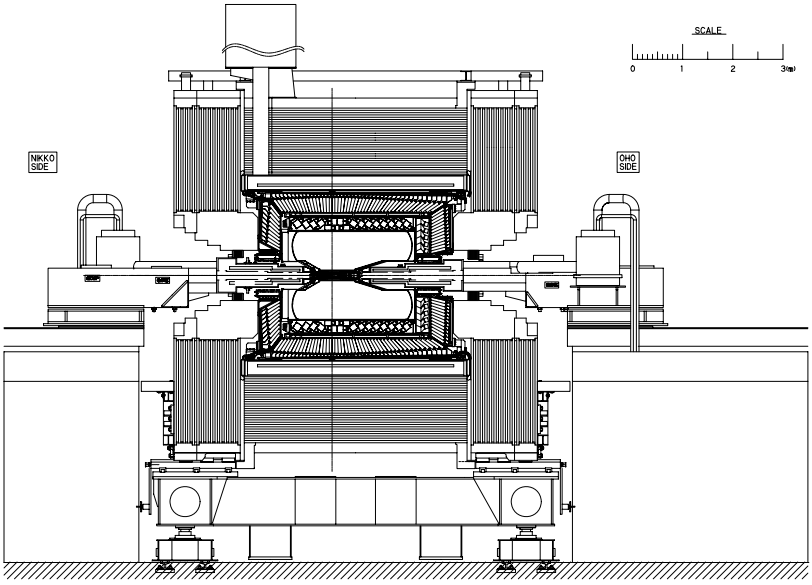

Figure 2.6: A side view of the Belle detector.

Table 2.1: Performance parameters of each sub-detector of Belle. There are two configurations of the inner detector, SVD1 and SVD2, corresponding to a 3-layer and a 4-layer SVD with a smaller beam pipe, respectively.

Detector	Type	Configuration	Readout	Performance
Beam pipe for SVD1	Beryllium double wall	Cylindrical, r=20mm, 0.5/2.5/0.5(mm)=Be/He/Be w/ He gas cooled		
Beam pipe for SVD2	Beryllium double wall	Cylindrical, r=15mm, 0.6/0.5/0.35(mm) =Be/PF200/Be		
SVD1	Double-sided Si strip	3-layers:8/10/14 ladders Strip pitch: 25(p)/50(n) μm	ϕ:40.96k z:40.96k	$\sigma_z \sim 66\mu m$
SVD2	Double-sided Si strip	4-layers:6/12/18/18 ladders Strip pitch: 75(p)/50(n) μm(layer1-3) 73(p)/65(n) μm(layer4)	ϕ:55.296k z:55.296k	$\sigma_z \sim 56\mu m$
CDC for SVD1	Small cell drift chamber	Anode:50 layers Cathode:3 layers r=8.3-87.4cm $-77 \leq z \leq 160$cm	Anode:8.4k Cathode:1.8k	$\sigma_{r\phi} = 130\mu$m $\sigma_z = 200 \sim 1400\mu$m $\sigma_{p_t}/p_t = 0.3\% \sqrt{p_t^2+1}$ $\sigma_{dE/dx} = 6\%$
CDC for SVD2	Small cell drift chamber	Anode:49 layers No cathode layer r = 10.4 - 87.4 cm $-77 \leq z \leq 160$cm	Anode:8.5k	
ACC	Silica aerogel	960 barrel/228 end-cap FM-PMT readout		$N_{p.e.} \geq 6$ K/π separation: $1.2 < p < 3.5$GeV/c
TOF	Scintillator	128 ϕ segmentation r=120cm,3cm long	128×2	σ_t=100ps K/π separation:
TSC		64 ϕ segmentation	64	up to 1.2GeV/c
ECL	CsI (Towered-structure)	Barrel:r=125-162cm End-cap:z= -102cm and +196cm	6624 1152(F) 960(B)	$\sigma_E/E = 1.3\%/\sqrt{E}$ $\sigma_{pos} = 0.5\text{cm}/\sqrt{E}$ (E in GeV)
KLM	Resistive plate counters	14 layers (5cm Fe + 4cm gap) 2RPCs in each gap	θ :16k ϕ :16k	$\Delta\phi = \Delta\theta$=30mrd for K_L $\sim 1\%$ hadron fake
Magnet	Super conducting	Inner radius=170cm		B=1.5T

beryllium walls is 0.3% of a radiation length. The inner radius of the beam pipe was changed to 1.5 cm in SVD2, and the cooling material is also changed from helium gas to Paraffin liquid.

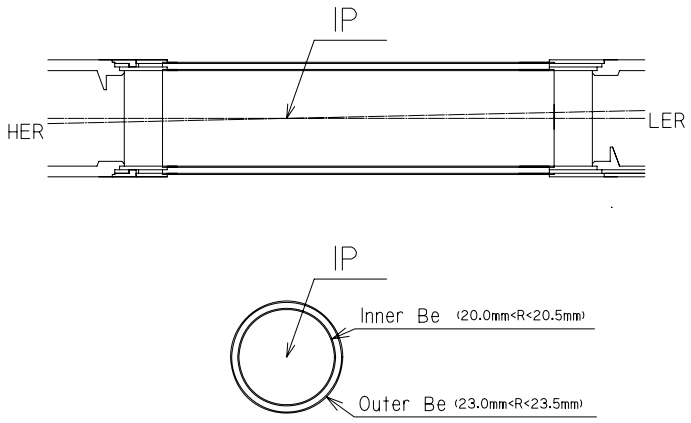

Figure 2.7: The cross section of the beam pipe at the IP.

The SVD [24] is designed to measure the decay vertices of B mesons. This information is very important for observation of time-dependent CP asymmetries in the decays of B mesons. In addition, the vertex detector is useful for identifying and measuring the decay vertices of D and τ particles.

Fig. 2.8 shows side and end view of SVD1. It consists of three layers of silicon sensors and covers a polar solid angle $23^\circ < \theta < 139^\circ$, which corresponds to 86% of the full solid angle. The radii of the three layers are 30, 45.5 and 60.5 mm. Each layer is made of double-sided silicon strip detectors (DSSDs) with boron-nitride support ribs sandwiched by carbon-fiber reinforced plastic. Each DSSD with a thickness of 300 μm consists of 1280 sense strips and 640 readout pads on opposite sides.

Fig. 2.9 shows the configuration of SVD2 [25]. It has four layers with radii of 20, 43.5, 70 and 88 mm. The angular acceptance is expanded to $17^\circ < \theta < 150^\circ$ (same as CDC).

When charged particles traverse a DSSD, electron-hole pairs are produced and then collected at the sense stripes. This signal will appear only on a few z and

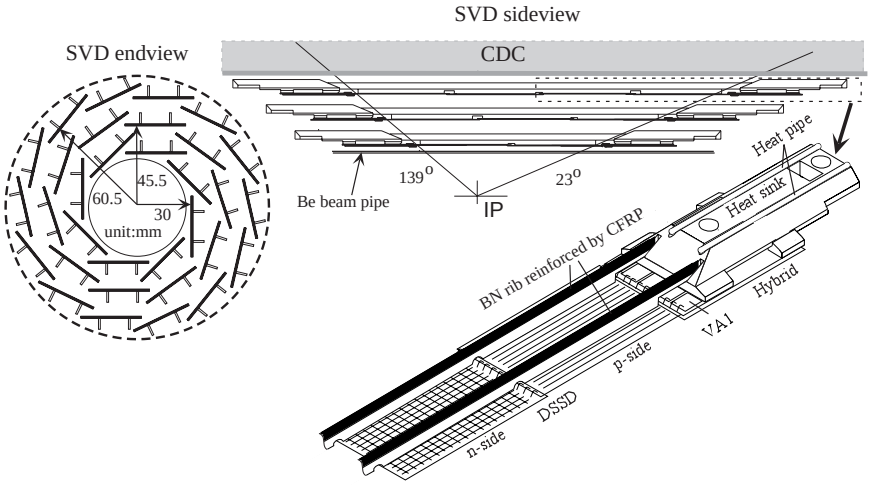

Figure 2.8: Detector configuration of SVD1.

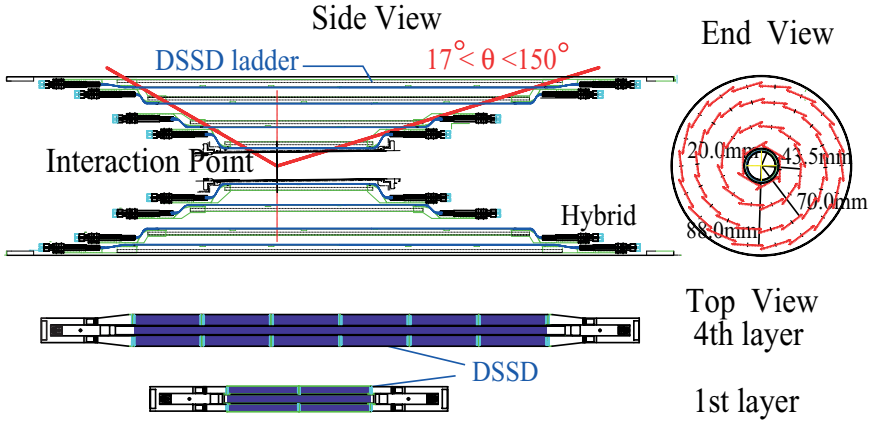

Figure 2.9: Detector configuration of SVD2.

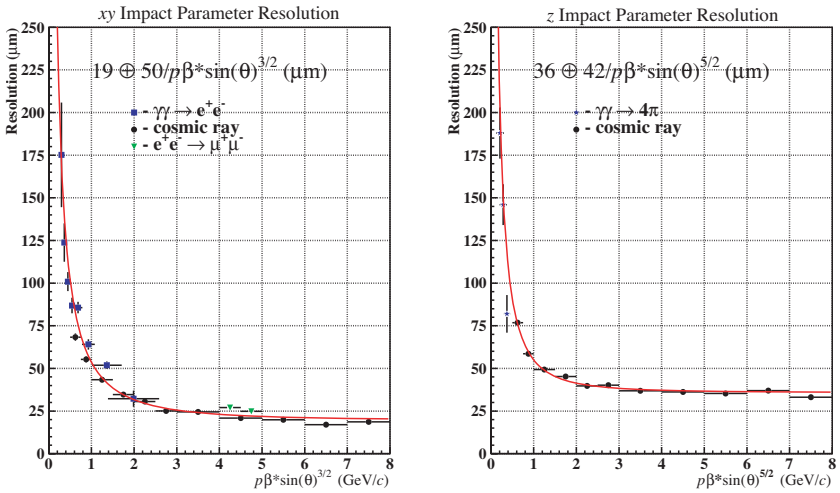

Figure 2.10: The performance of SVD1.

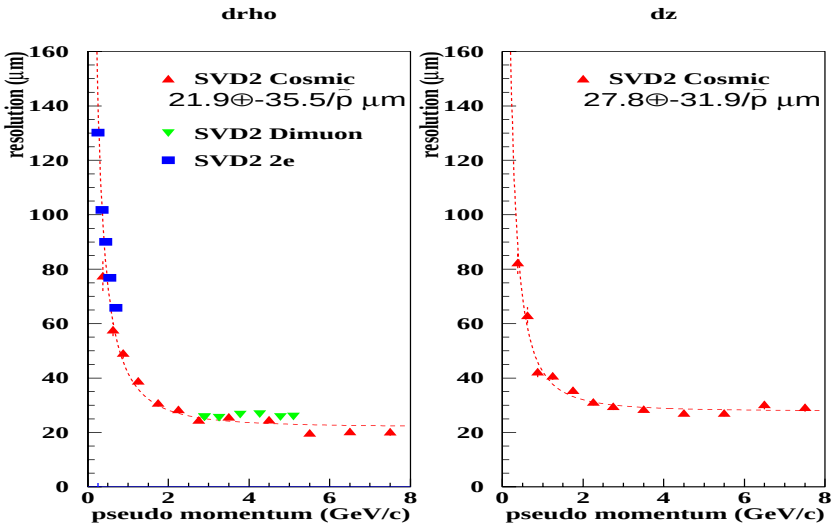

Figure 2.11: The performance of SVD2.

ϕ strips. Thus, three-dimensional (3D) hits information is obtained. The impact parameter resolution which are directly related to the vertex resolutions, in function of the momentum and angular dependence is shown in Fig. 2.10 and 2.11 for SVD1 and SVD2, respectively.

2.2.2 CDC — Central Drifter Chamber

The main role of CDC [26] is to efficiently reconstruct charged particle tracks and precisely determine their momenta. In addition, CDC also provides important information for the trigger system and particle identification (PID) information from the energy loss (dE/dx) of the charged particles.

The configuration of the CDC is shown in Fig. 2.12. It provides a polar angular coverage of $17^\circ < \theta < 150^\circ$, which corresponds to 92% of the full solid angle. The inner and outer radii are 83 and 880 mm, respectively. The CDC consists of 50 cylindrical sense wire layers, each containing between three and six either axial or small-angle-stereo layers, and 3 cathode strip layers (in the SVD1 configuration). In total, there are 8400 drift cells, each of which contains one sense wire at positive voltage surrounded by eight field wires in ground voltage. An example of the cell arrangement at the inner-most radii is shown in Fig. 2.13. The cathode strips provide z-coordinate measurements at the inner-most radii (which was used for trigger purpose only).

In the summer of 2003, the inner part structure of CDC has been modified jointly with the upgrade of SVD. The three inner layer with cathode strips were removed to make the space for the upgraded SVD with larger radius. Instead, we have installed two layers of small cells, which we call small-cell CDC (sCDC). The inner radius after the modification is 104 mm, while the other geometry is unchanged.

A gas mixture of 50% Helium and 50% Ethane is used to fill in the CDC. The use of a low-Z gas is to minimize multiple Coulomb scattering. Charged tracks passing through the drift chamber ionize gas molecules along their path. The ionized electrons drift forwards the sense wires, at a velocity which saturates at ~ 4 cm/μs, and depends relatively weakly on the electric field strength. Only when the electrons come very

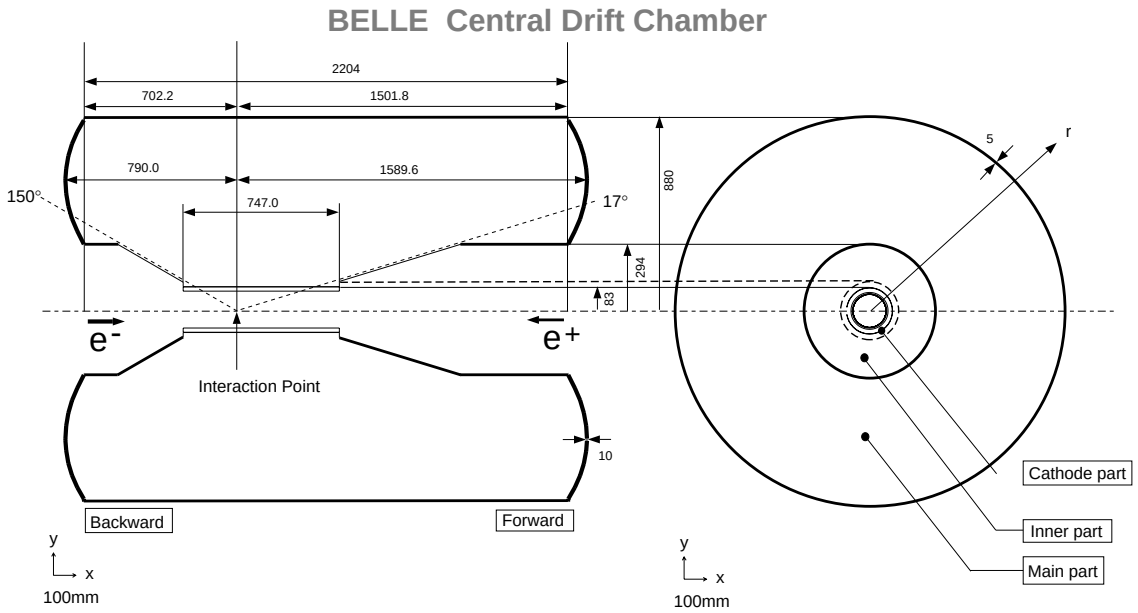

Figure 2.12: Overview of the CDC structure. The lengths in the figure are in units of mm.

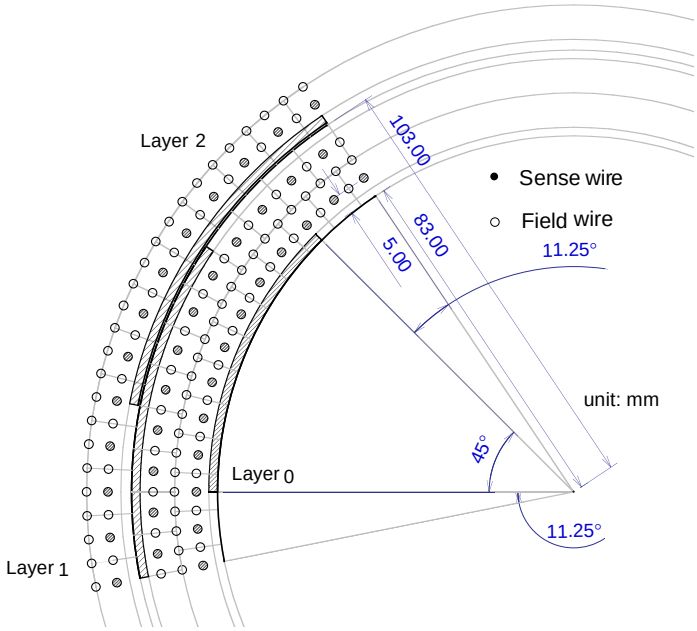

Figure 2.13: Cell structure and the cathode sector configuration.

close to the sense wires, does their energy become large enough to liberate fresh ions, creating an ionization avalanche which total charge proportional to the gas gain and the amount of primary ionization. Both the pulse time and the integrated charge of this signal are recorded and used.

By combining the information from many sense wires, the trajectory in the $x-y$ plane can be reconstructed. Stereo wires, which run at a small angle with respect to the other wires in the chamber, provide additional z information. The curvature of the track's $x-y$ plane projection in the 1.5 T magnetic field, is used to measure the transverse momentum of the track. The CDC provides a $r-\phi$ spatial resolution of approximately 130 μm. The transverse momentum p_t resolution is measured to be $(0.201 p_t \oplus 0.290/\beta)\%$ (p_t in GeV/c). It is from a fit to data points from cosmic rays indicated with the solid curve in Fig. 2.14.

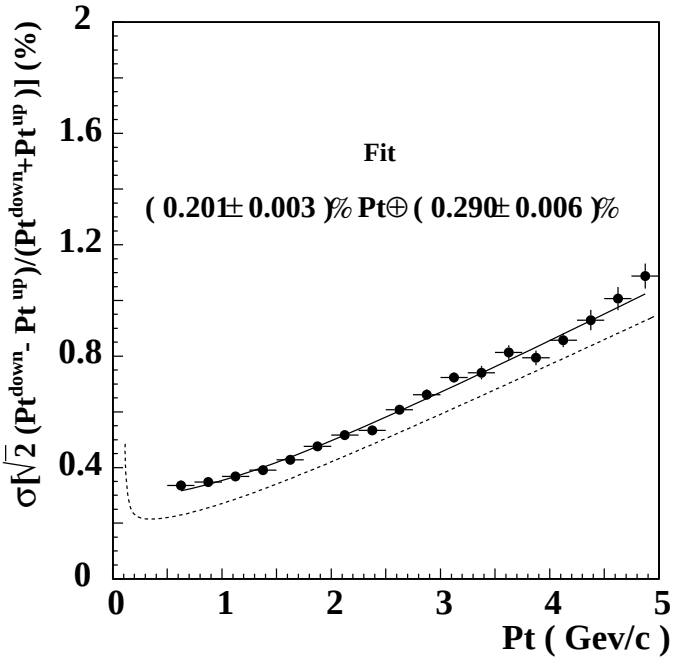

Figure 2.14: p_t dependence of p_t resolution for cosmic-rays.

The time integrated charge of the pulse can be used for PID. Since the energy loss (dE/dx) is a function of the velocity (β) of the particle, it can be used to distinguish particles with the same momentum but different masses. Fig. 2.15 shows a scatter

plot of measured dE/dx versus the particle momentum, together with expected energy losses for different particle species. The dE/dx resolution is measured to be 7.8% in the momentum range from 0.4 to 0.6 GeV/c. And the dE/dx measurement provides over 3σ separation between K and π for momenta below 0.8 GeV/c and 2σ separation for momenta above 2.0 GeV/c.

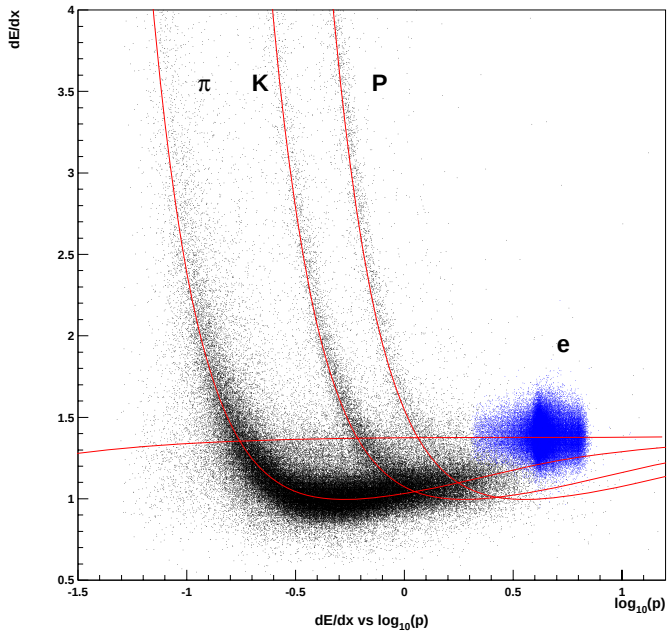

Figure 2.15: Truncated mean of dE/dx versus momentum observed in collision data.

2.2.3 ACC — Aerogel Cherenkov Counter

An array of silica aerogel Cherenkov counter (ACC) [27] is used as a part of the Belle PID system to extend the momentum coverage beyond the reach of the dE/dx measurement by CDC and the time-of-flight measurement by TOF. When a charged particle is moving in a medium with refractive index n, it will emit Cherenkov light if its velocity is greater than the threshold c/n, or, $\beta > 1/n$. For a fixed n, the threshold momentum is proportional to their masses, so there are regions where the pion produces Cherenkov light while the kaon does not. And K/π separation in

a desired momentum region can be achieved by selecting media with appropriate refractive index values [28].

The configuration of the silica aerogel Cherenkov counter system is shown in Fig. 2.16. ACC consists of 960 counter modules segmented into 60 cells in the ϕ direction for the barrel part and 228 modules arranged in 5 concentric layers for the end-cap part, covering the polar angular ranges $34° < \theta < 127°$ and $17° < \theta < 34°$ respectively. The refractive indices of aerogels are between 1.01 and 1.03, depending on their polar angle region to provide 3σ separation in the momentum region $1.0 < p_K < 3.6$ GeV/c. The typical counter module consists of silica aerogel filled in 0.2 mm-thick aluminum boxes and viewed with one or two fine-mesh photomultiplier tubes (FM-PMTs). The FM-PMTs can be operated well in a 1.5T magnetic field. Fig.2.17 shows a schematic drawing of the ACC module.

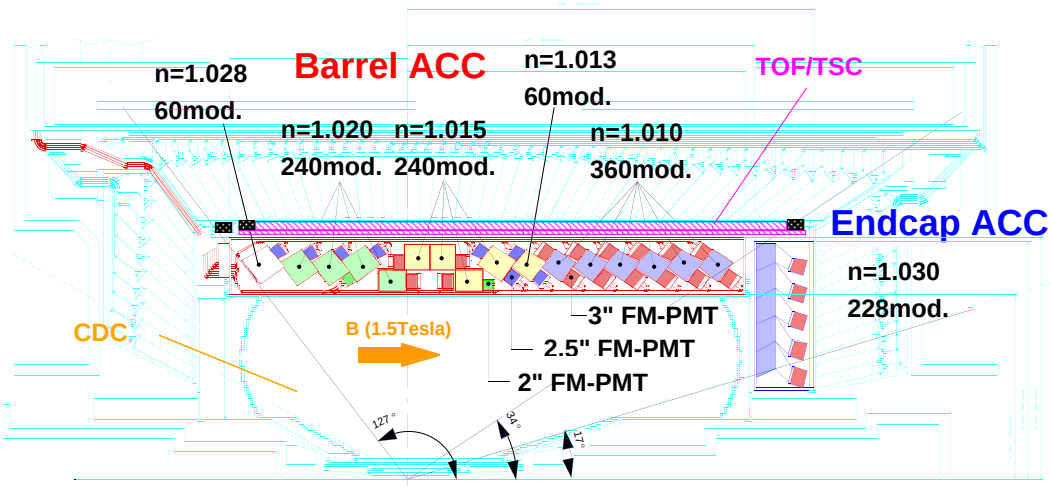

Figure 2.16: The configuration of ACC and TOF.

Fig. 2.18 shows the number of photo-electrons detected for kaons below threshold and electrons above threshold. For kaons of momenta from 1.5 GeV/c to 4.0 GeV/c, the ACC can provide a good K/π separation with a kaon detection efficiency of 73% and the pion fake rate of 7%.

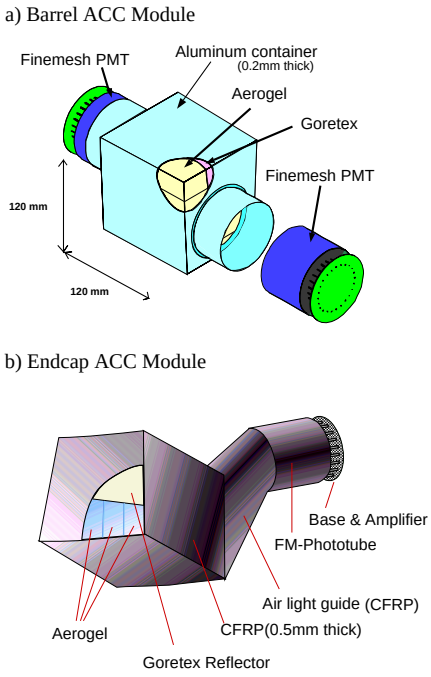

Figure 2.17: Schematic drawing of a typical ACC counter module: (a) barrel and (b) end-cap ACC.

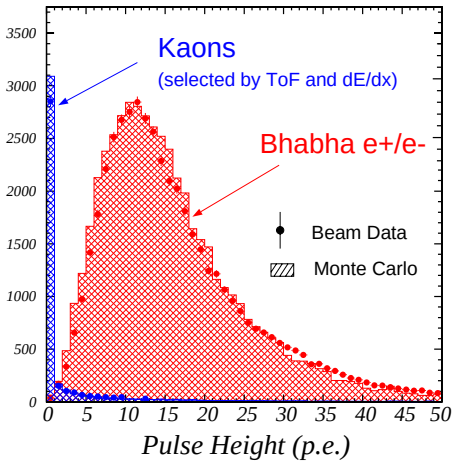

Figure 2.18: Pulse-height spectra in units of photoelectrons observed by barrel ACC for electrons and kaons. Kaon candidates were obtained by dE/dx and TOF measurements. The Monte Carlo expectations are superimposed.

2.2.4 TOF — Time-of-Flight Counter

For the same momentum, a heavy particle will travel slower than a light particle. Thus, time-of-flight (TOF) system can identify particles of different masses by measuring their flight time differences. In addition, TOF system also provide fast timing signals for trigger system.

The TOF system consists of 64 modules, each consisting of two ϕ-adjacent plastic scintillation TOF counters, separated by a 1.5 cm radial gap from a trigger scintillation counter (TSC), which cover a polar angle range from 34° to 120°. A module of TOF is shown in Fig. 2.19. The modules are located at 1.2 m radius, outside the ACC in the detector barrel, as shown in Fig. 2.16.

A charged particle traversing a scintillation counter will excite molecules in its path, resulting in the subsequent emission of scintillation photons. The photons are travelling by internal refection inside the scintillation counter until they are read out with fine-mesh-dynode photomultiplier tubes (FM-PMTs) [29] at the ends.

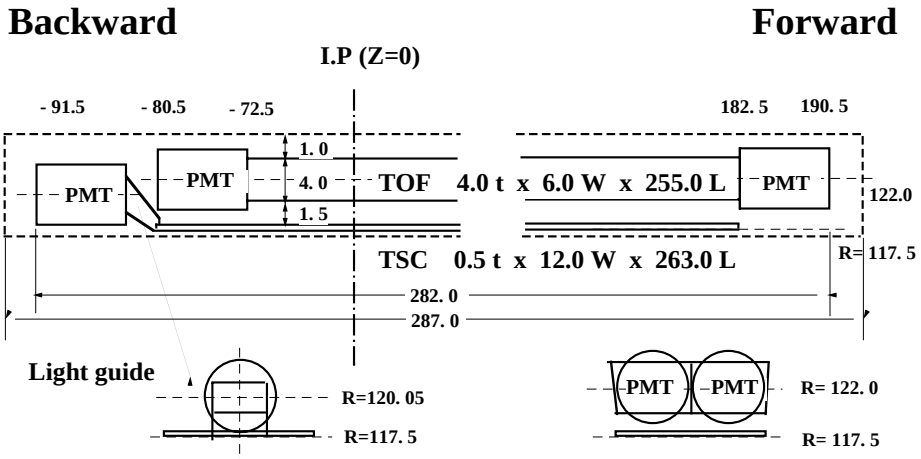

Figure 2.19: Dimensions of a TOF/TSC module. The lengths in the figure are in units of cm.

The performance of TOF is shown in Fig. 2.20. The resolution is about 100 ps with a small z dependence. Fig. 2.21 shows the mass distribution for particles of momenta below 1.2 GeV/c in hadron events. The K, π, p signals are clearly separated. The TOF system gives 2σ K/π separation for particle momenta up to

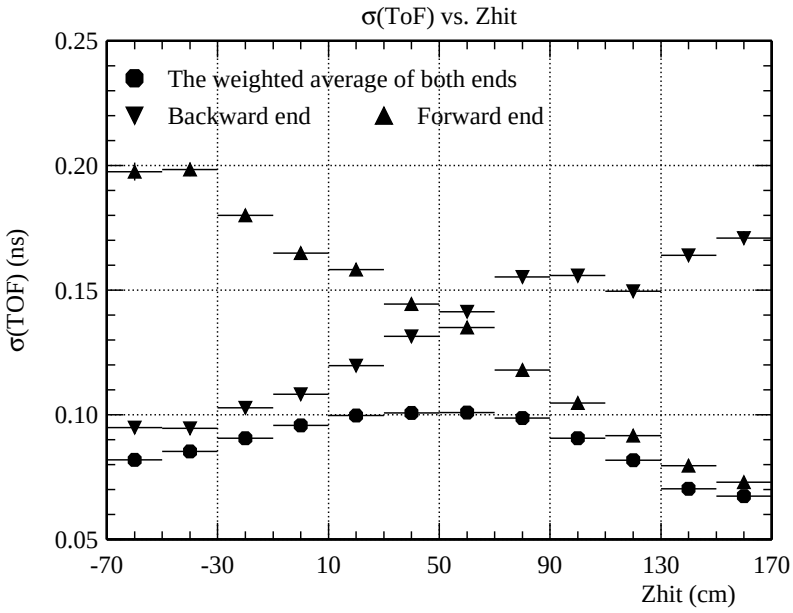

Figure 2.20: Time resolutions of forward and backward PMTs and of the weighted average time as a function of z for μ pairs after calibration.

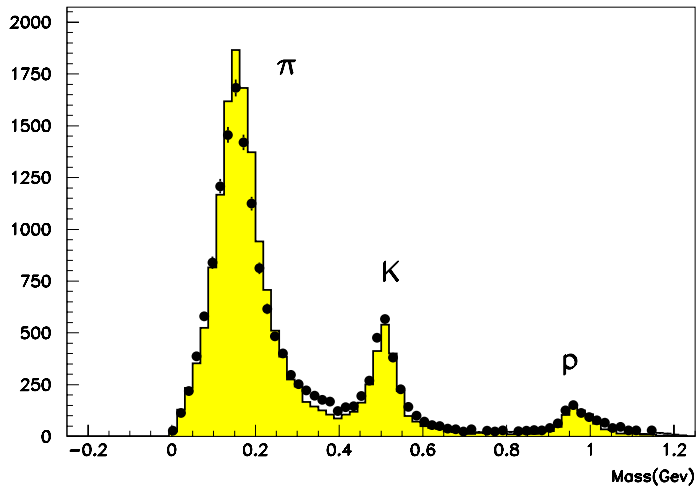

Figure 2.21: Mass distribution from TOF measurements for particle momenta below 1.2 GeV/c. The data points are in good agreement with the Monte Carlo prediction (histogram) obtained by assuming $\sigma_{TOF} = 100$ ps.

1.25 GeV/c.

2.2.5 ECL — Electromagnetic Calorimeter

The electromagnetic calorimeter (ECL) [30] is designed mainly to detect photons and to identify electrons, but can also be used to detect K_L's and minimum ionizing particles. The ECL consists of 8736 CsI(Tl) crystals, arranged in a barrel part, and end-cap parts in the solenoid magnet as shown in Fig. 2.22, and covering the polar angle region $17° < \theta < 150°$. Each crystal has a tower-like shape and points roughly towards to the interaction point. The crystal has a length of 300 mm, which corresponds to 16.2 radiation lengths to avoid shower leakages in the rear.

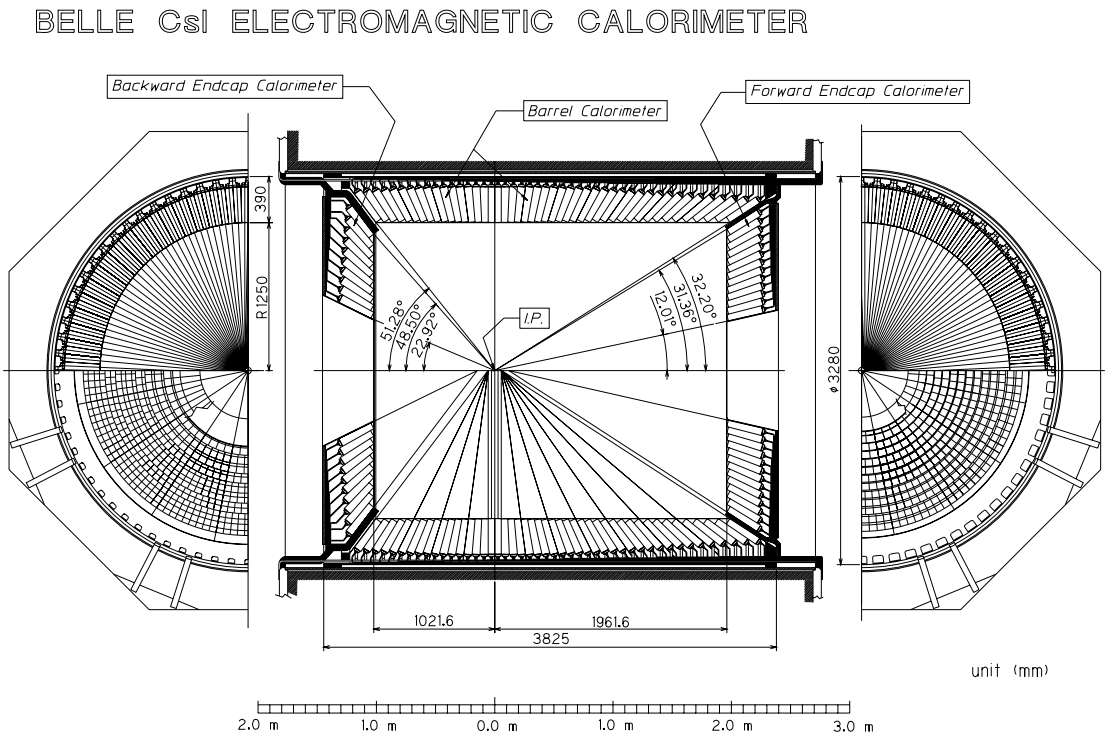

Figure 2.22: ECL configuration.

At high energy, an electron loses energy by bremsstrahlung and a photon loses energy by electron-position pair production. The repetition of these processes produces electromagnetic showers in the calorimeter. Finally the energy of a shower is

measured from the amount of the scintillation photons detected by photo-diodes.

A shower in the ECL that is isolated from any tracks is identified as a neutral shower. The ECL energy resolution is measured to be

$$\frac{\sigma_E}{E} = \left(1.34 \oplus \frac{0.066}{E} \oplus \frac{0.81}{E^{1/4}}\right) \% \tag{2.1}$$

with the beam test.

2.2.6 Superconducting Solenoid

A superconducting solenoid provides a magnetic field of 1.5 T in a cylindrical volume of 3.4 m in diameter and 4.4 m in length [31].

The axial magnetic field makes charged particle to travel in a helix track, with the $x - y$ projections of its trajectory being a circle of radius R, related to the field B by

$$R = \frac{p_T}{0.3qB} \tag{2.2}$$

where q is the charge of the particle (in multiples of the electron charge), p_T is the particle's transverse momentum (GeV/c).

Thus, we can determine a charged particle's momentum and its charge from the curvature of its trajectory in the CDC and SVD.

2.2.7 KLM — K_L and Muon Detector

A K_L and Muon Detector (KLM) [32] is designed to identify K_L's and muons with high efficiency over a broad momentum range greater than 600 MeV/c. It is composed of glass-resistive plate counters (RPCs) sandwiched between 4.7-cm-thick iron plates. There are 15 detector layers and 14 iron layers in the octagonal barrel region and 14 detector layers in each of the forward and backward end-caps. The barrel and end-caps region of the KLM cover an polar angular range from 20° to 155°.

RPCs have two parallel plate electrodes with high bulk resistivity separated by a gas-filled gap. An ionizing particle traversing the gap initiates a streamer in the gas that results in a local discharge, which induces a signal on external pickup stripes to record the location and the time of the ionization.

A detected shower that does not match any extrapolated tracks is identified as K_L. The location of the shower determines the direction of the K_L, but fluctuations in the size of the shower do not allow a useful measurement of the K_L energy. Muons can be discriminated from strongly interacting hadrons based on the trajectory range and transverse scattering, because muons travel much further with small deflection in average.

2.2.8 EFC–Extreme Forward Calorimeter

The role of the Extreme Forward Calorimeter (EFC) is a beam monitor for the KEKB operation, a luminosity monitor, to improve the experimental detection performance. It consists of 320 radiation hard BGO (Bismuth Germinate, $Bi_4Ge_3O_{12}$) crystals. They are attached to the cryostat of the superconducting compensation solenoid magnets, and surround the beam pipe outside the interaction point in the forward and backward region. The EFC extends the coverage of the ECL to the polar angle regions 6.5° to 11.5° and 163.3° to 171.2°.

2.2.9 Trigger & Data Acquisition (DAQ)

The Belle trigger system [33] is designed to keep the maximum efficiency for $B\overline{B}$ events and suppress the background events. The system consists of three levels: level one hardware trigger (L1), level three online software trigger (L3), and level four offline trigger (L4).

The L1 trigger consists of sub-detector trigger system and global decision logic (GDL). Fig. 2.23 shows the schematic diagram for Belle L1 trigger. The trigger signals from subdectors are combined in GDL, and GDL makes the final decision to initiate the data taking with 2.2 μsec from beam crossing. Charged track information from CDC and energy information from ECL are prepared for hadronic events. These two redundant triggers keep more than 99.5% efficiency for $B\overline{B}$ events. Then the common stop signals are sent to each sub-detector. The typical trigger rate is 200-250 Hz.

The overview for Belle data acquisition (DAQ) system is shown in Fig. 2.24. The DAQ system is segmented into 7 subsystems running in parallel to keep the dead time

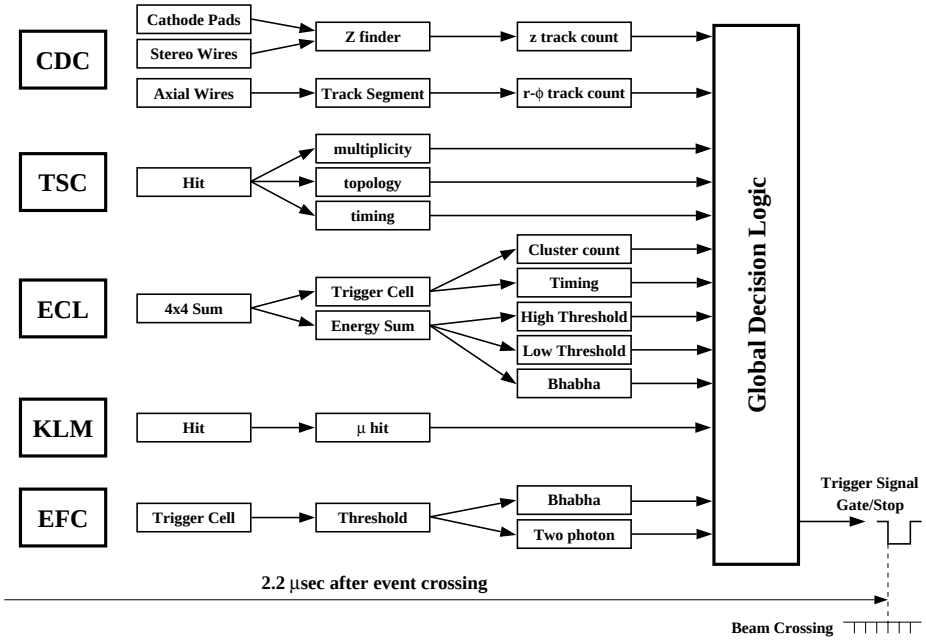

Figure 2.23: Belle Level one (L1) trigger.

fraction less than 10% up to the maximum trigger rate of 500 Hz. The sub-detector signals are converted to timing signals by Q-to-T converter except for KLM and SVD then sent to TDC readout system. KLM provides the time-multiplexed information on a signal line, and the signal is sent to TDC directly. The TDC readout system is controlled by VME and FASTBUS. The SVD signal is sent to flash ADC's (FADC) and data are gathered in the memory module.

All the data collected is sent to Event Builder. The Event Builder gather the data from sub-dececters to form the "event-by-event" data and sent it to the online computer farm. The online computer transforms the event data into offline event format with background filtering based on L3 information. Then the data is sent to a mass storage system which is located 2 km away and the data is transferred by optical fiber. The data for typical event is 30 KB corresponding to the maximum data rate of 15 MB/s.

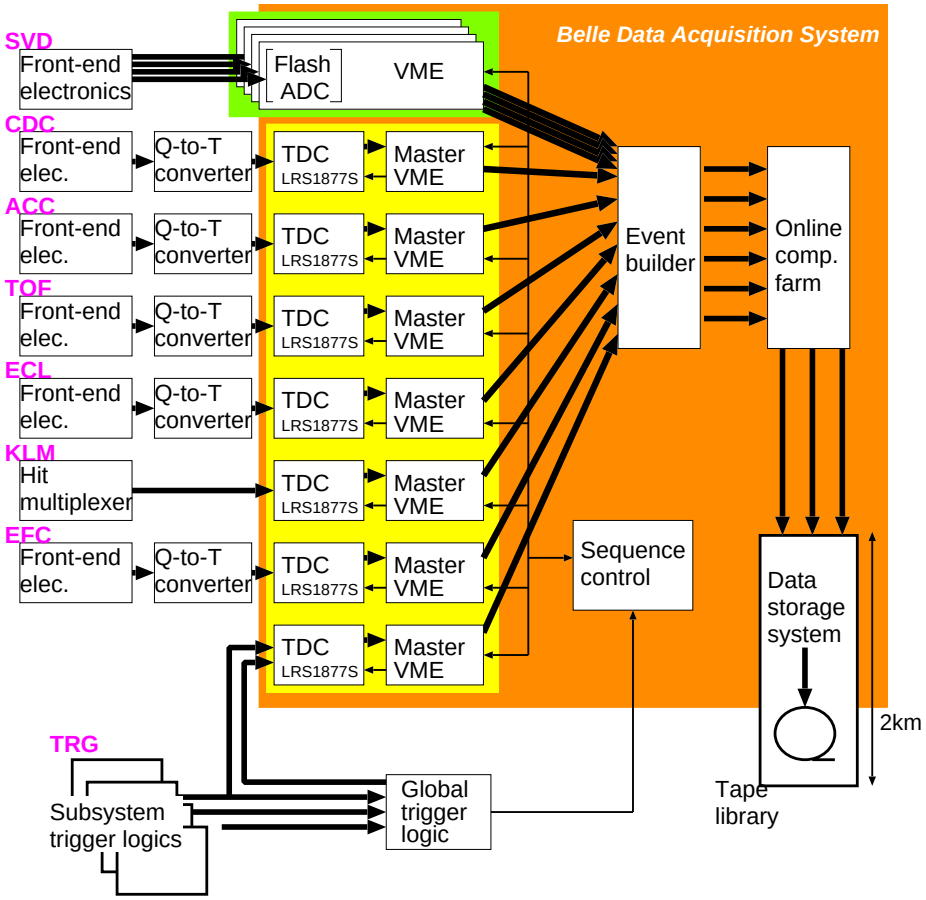

Figure 2.24: The overview for Belle data acquisition system.

Chapter 3

Event Reconstruction

3.1 Particle Identification

3.1.1 Kaon-pion Separation

The kaon-pion separation in the Belle experiment is based on three nearly-independent measurements–dE/dx measurement by the CDC, time of flight measurement by the TOF and the number of Cherenkov photons in the ACC–each of them yields good separation between particle species in a different momentum and angular region. It is therefore necessary to combine the sub-detector information in some way, to allow kaon-pion separation in physics analysis over a range of momenta and polar angles.

One practical approach is to use a likelihood method and form a single cut variable, based on responses from the sub-detectors for each of kaon and pion. In general, this approach gives better signal/background separation than the box-cut approach, where independent sharp cuts are applied to the sub-detector outputs. Moreover, optimization of kaon-pion separation cuts in user analysis become easier.

Kaon-pion separation is based on the likelihood of the detector response being due to an hypothesized signal particle species, compared to the likelihood for an assumed background particle species. This is expressed as a likelihood ratio

$$\mathcal{R}(i:j) = \frac{P_i}{P_i + P_j} \tag{3.1}$$

Where P_i is the particle-ID likelihood calculated for the signal particle species and P_j for the background particle species. Clearly $\mathcal{R}(i:j)$ is distributed on the interval [0,1]. $\mathcal{R}(i:j) = 0.5$ when the kaon-pion separation system cannot distinguish between the hypotheses i and j. The true particle-ID probability corresponding to a fixed cut depends on the sample being studied, and is in general a function of momentum and polar angle within that sample. It is important to note that the signal efficiency and fake rate for any cut are also functions of momentum and polar angle.

Each likelihood P_i is the product of the three sub-detector likelihoods:

$$P_i = P_i^{dE/dx} \times P_i^{\mathrm{TOF}} \times P_i^{\mathrm{ACC}} \tag{3.2}$$

The likelihood functions for the three sub-detectors, $P_i^{dE/dx}$, P_i^{TOF} and P_i^{ACC}, are calculated as follows:

- $d\mathbf{E}/d\mathbf{x}$

  In the dE/dx reconstruction module, the χ^2 value for each particle hypothesis is calculated as

  $$\chi^2 = (\frac{(dE/dx)^{\mathrm{measured}} - (dE/dx)^{\mathrm{expected}}}{\sigma_{dE/dx}}) \tag{3.3}$$

  where $(dE/dx)^{\mathrm{measured}}$ and $(dE/dx)^{\mathrm{expected}}$ are the measured and expected dE/dx values, respectively, and $\sigma_{dE/dx}$ is the (expected) resolution of the dE/dx measurement. Then the likelihood is calculated, assuming a Gaussian distribution:

  $$P^{dE/dx} = \frac{e^{-\frac{1}{2}\chi^2}}{\sqrt{2\pi}\sigma_{dE/dx}}. \tag{3.4}$$

- **TOF**

  The likelihood calculation is based on the measured and expected times for each photo-tube. The TOF χ^2 is constructed by taking the difference between a two-vector containing the observed times in the two photo-tubes of a counter and one containing the predicted times

  $$\Delta_i = t_i^o - t_i^p, \tag{3.5}$$

where $i = 0,1$ refers to the two ends of the counter. The 2×2 error matrix for Δ (call it E) is evaluated by summing the contributions due to the uncorrelated uncertainty in the digitized times in the two photo-tubes and the correlated uncertainty due to the calculated time-of-flight from the tracking results. The χ^2 for one counter is then given by

$$\chi^2 = \Delta^T E^{-1} \Delta. \tag{3.6}$$

If a track passes through the edges of two counters, the counter χ^2's are summed to give the total χ^2 for the track (ignoring the correlation between the times in the two counters). Finally, the likelihood is calculated by evaluating

$$P^{TOF} = \frac{e^{-\frac{1}{2}\chi^2}}{\prod_{i=1}^{ndf} \sqrt{2\pi}\sigma_i}. \tag{3.7}$$

where *ndf* is the number of PMT times that are included in the χ^2.

- **ACC**

  In contrast to dE/dx and the TOF counters, the ACC is basically an on-off device, where the observed signal (number of photo-electrons, N_{pe}) is either zero, or distributed according to small-number statistics. For sub-threshold particles, the spectrum peaks at zero with a background tail due to δ-ray Cherenkov or light emission in the Goretex reflector. For above-threshold particles, the spectrum can be interpreted as a distribution of photo-electrons at the photo-cathode (following the Poisson distribution), smeared by multiplicative amplification through fine-mesh dynodes. The likelihood is given by comparing the observed N_{pe} with a threshold value, N_{pe}^{th}, using the expected efficiency ϵ at the measured momentum:

$$P^{ACC} = \epsilon(N_{pe} \geq N_{pe}^{th}) \tag{3.8}$$

$$P^{ACC} = 1 - \epsilon(N_{pe} \leq N_{pe}^{th}) \tag{3.9}$$

  The expected efficiency at the measured momentum for an assumed particle species, ϵ, is estimated by linear interpolation of efficiency values, which are evaluated at 18 β points and pre-stored in efficiency tables. The threshold,

N_{pe}^{th}, is chosen so that the maximum separation between below-threshold and relativistic particles is obtained. The efficiency table and the threshold value are prepared based on Monte Carlo simulations for each of 10 polar angular regions, corresponding to each type of counter module.

When information from one of the sub-detector is not available for the examined track, 0.5 is assigned for the sub-detector likelihood for any particle species. Fig. 3.1 shows the momentum region in which the sub-detector can well discriminate a kaon from a pion.

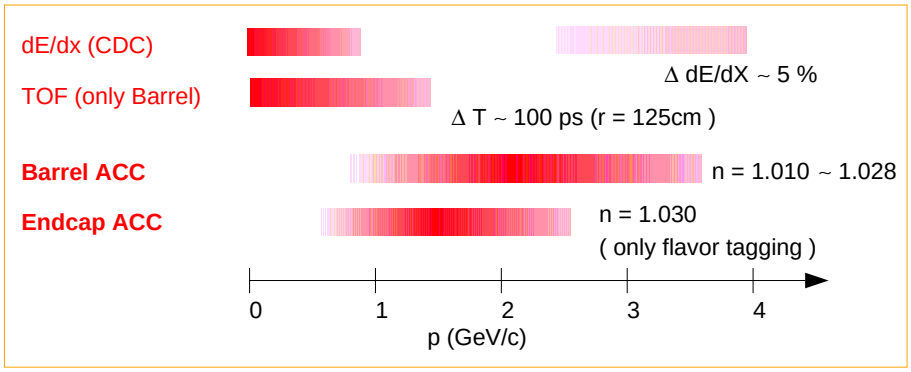

Figure 3.1: Momentum region favored for different sub-detector for kaon-pion separation.

The validity of the kaon-pion separation is demonstrated using the data of the charm decay chain of $D^{*+} \to D^0\pi^+(D^0 \to K^-\pi^+)$. In the decay chain, we can use the charge of the slow pion from the D^{*+} to determine the kaon and pion from $D^0 \to K^-\pi^+$ decay, which allows us directly measure the performance of the kaon-pion separation. Fig. 3.2 shows a two-dimensional distribution of the likelihood ratio and the measured momenta for the kaon and pion tracks. The figure demonstrates the clear separation between kaons and pions up to around 4 GeV/c. The measured kaon efficiency and pion fake rate in the barrel region are plotted as functions of the track momentum in Fig. 3.3, where a selection criterion of $\mathcal{R}(K:\pi) > 0.6$ is applied.

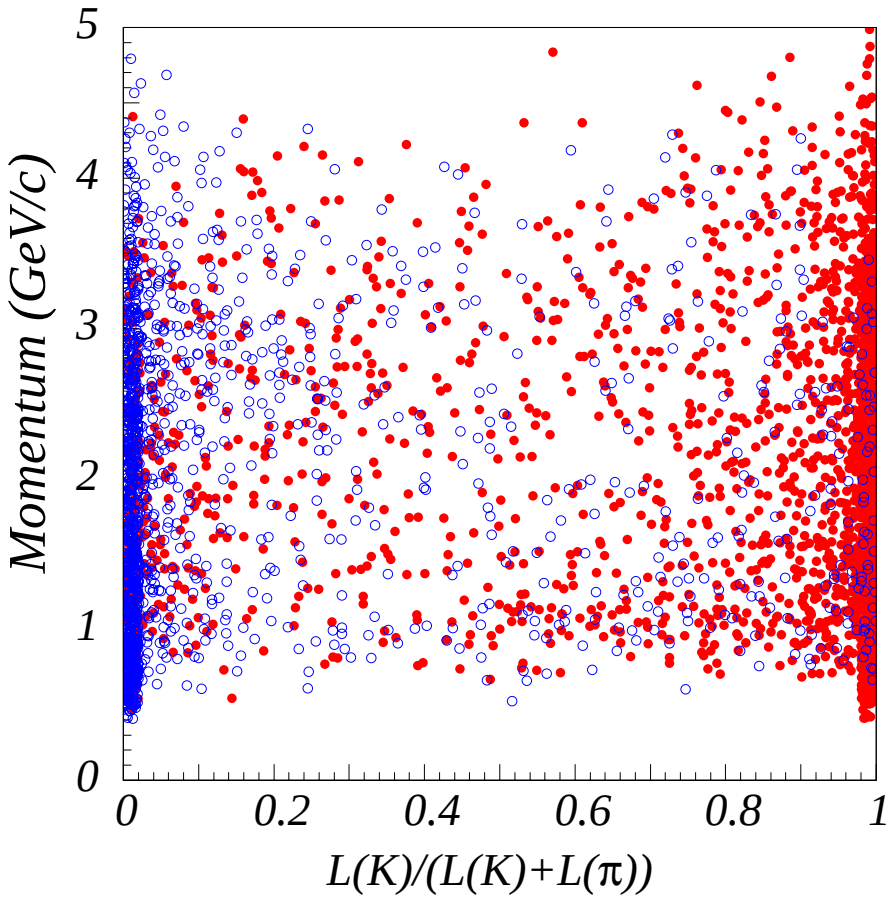

Figure 3.2: A dcatter plot of the track momentum (vertical axis) and the likelihood ratio $\mathcal{R}(K:\pi)$ (horizontal axis) for $K^{\pm}$ (closed circle) and $\pi^{\pm}$ (open circle) obtained from the data of $D^{*+} \to D^0\pi^+(D^0 \to K^-\pi^+)$ decays.

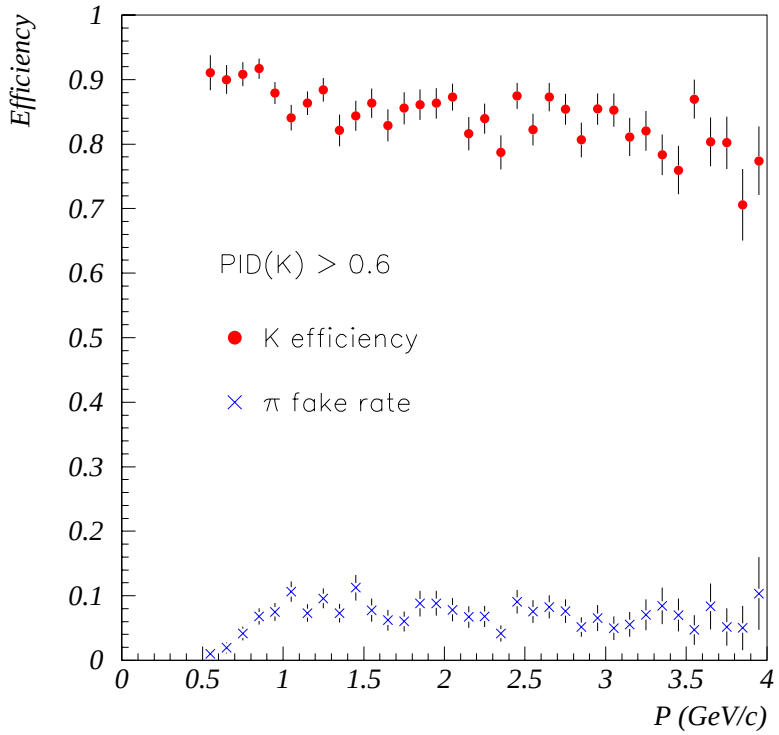

Figure 3.3: K efficiency and π fake rate in the barrel region measured using the data of $D^{*+} \to D^0\pi^+(D^0 \to K^-\pi^+)$ decays. The selection criterion of $\mathcal{R}(K:\pi) > 0.6$ is applied here.

3.1.2 Electron Identification

Electron identification (EID)[34] at Belle has two approaches: the first exploits the difference in the electromagnetic showers induced by the electrons and the hadronic showers induced by the pions and other hadrons; the second uses the difference of vilocity for electrons and hadrons of the same momentum. The following discriminants are used for EID:

- the ratio of energy deposited in ECL (E) and charged track momentum (p)measured by CDC: E/p.

  The E/p is use as a powerful discriminant to distinguish electrons from hadrons. Since the electron deposits almost all energy in ECL, the electron's E/p becomes close to unity. The deposit energy of hadrons in ECL is smaller than their momentum ($E < p$). Fig. 3.4 shows E/p distribution for electrons and charged pions in the momentum region $0.5 < p_{\rm lab} < 3.0$ GeV/c^2 and momentum dependence of E/p.

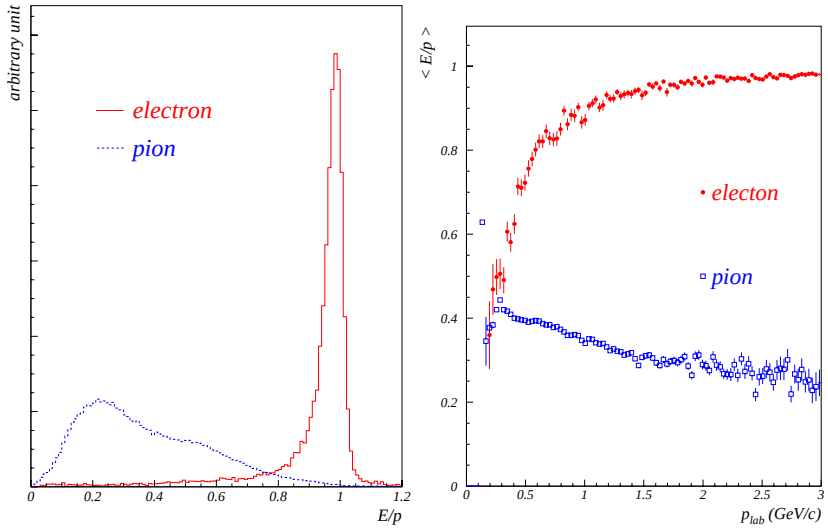

Figure 3.4: E/p distribution and momentum dependence of E/p for EID. Left: E/p for electrons and charged pions, Right: Momentum dependence of E/p for electrons and charged pions.

- transverse shower shape at ECL.

Since electromagnetic shower and hadronic shower have different shape in both transverse and longitudinal directions, this difference can be used as a significant discriminant. The shower shape in the transverse direction can be evaluated with $E9/E25$, which is defined as the ratio of energy summed in a 3×3 array of crystals surrounding the crystal at the center of the shower to that of a sum of a 5×5 array of crystals centered on the same crystal. Fig. 3.5 shows $E9/E25$ distributions for electrons and charged pions.

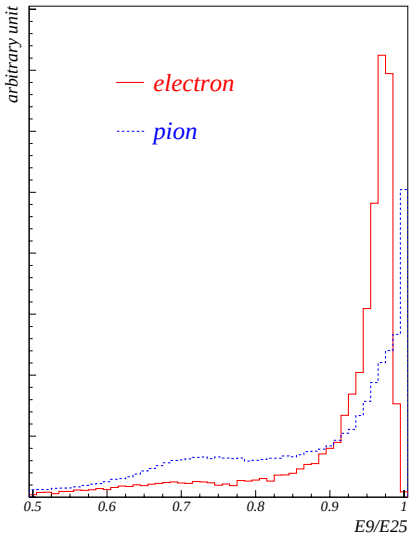

Figure 3.5: $E9/E25$ distributions for electrons and pions denoted by solid and broken histograms, respectively.

- the matching between a cluster at ECL and charged track position extrapolated to ECL. Electrons have good matching since the electromagnetic shower in the ECL develops along the electron track while hadrons have worse matching. A χ^2 is defined as

$$\chi^2 = \left(\frac{\Delta\phi}{\sigma_{\Delta\phi}}\right)^2 + \left(\frac{\Delta\theta}{\sigma_{\Delta\theta}}\right)^2 \tag{3.10}$$

  where $\Delta\phi(\Delta\theta)$ is a difference between cluster position and electron track position of azimuthal (polar) angle and σ is its width for electrons. Fig. 3.6 shows the position matching χ^2 distributions for electrons and pions.

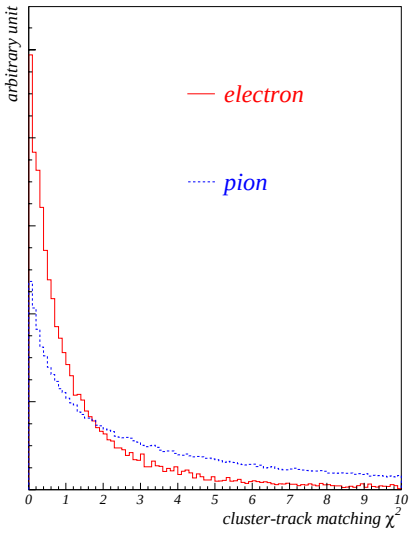

Figure 3.6: Cluster-track matching χ^2.

- dE/dx measured by CDC. Electrons and charged hadrons with the same momentum have different vilocities, which have a strong correlation with the dE/dx in CDC. This property can be used for EID. Fig. 3.7 shows the resulting dE/dx distributions for electrons and for pions.

- light yield in ACC. Electrons and hadrons with the same momentum have different vilocities and will yield different amount of light in ACC.

Information from the two approaches is combined into a single variable using a likelihood method. The likelihood from various discriminants are calculated based on probability density functions (PDFs). For each discriminant, the electron likelihood (L_e), and non-electron likelihood ($L_{\bar{e}}$), are separately calculated. Each likelihood is combined to form a likelihood ratio

$$\mathcal{R}_{\rm eid} = \frac{\Pi_{i=1}^{n} L_e(i)}{\Pi_{i=1}^{n} L_e(i) + \Pi_{i=1}^{n} L_{\bar{e}}(i)} \tag{3.11}$$

where i runs over each discriminant. The output of EID, $\mathcal{R}_{\rm eid}$, is used for discriminating between electrons and other particles. The efficiency of electron identification is greater than 90% and a hadron misidentification rate is $\sim 0.3\%$ for $p > 1$ GeV/c as shown in Fig. 3.8.

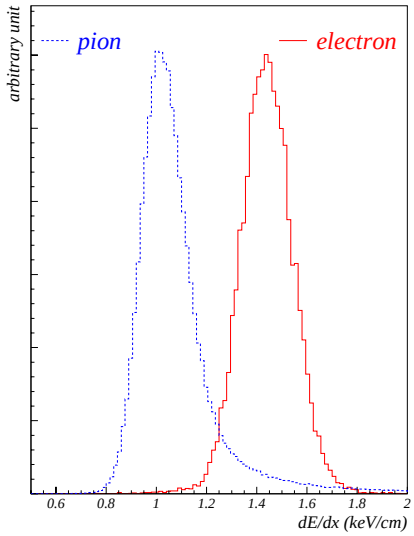

Figure 3.7: dE/dx for electrons and pions.

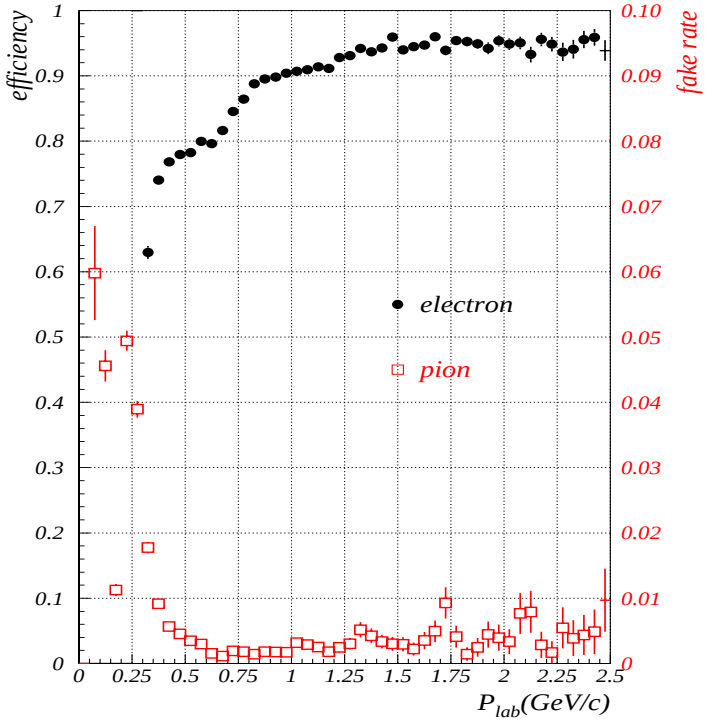

Figure 3.8: Electron identification efficiency and fake rate versus particle momenta.

3.1.3 Muon Identification

Muon identification [35] is based on the difference of interaction in material between muons and hadrons. Since a muon is a massive lepton, it deposits its energy only through the energy loss (ionization and atomic excitation). While an electron, the almost massless lepton, deposits its energy by the creation of an electromagnetic shower and a hadron deposits their energy through hadronic iteractions. Electrons fully diposit their energy in the ECL and rarely reach the KLM and thus can be easily distinguished from muons.

Muons are identified against hadrons as follows. A track is extrapolated from the CDC to the KLM and associated KLM hits are searched; a track is re-fitted with those associated KLM hits, assuming that a track goes through only with the energy loss and multiple scattering effects. We use the following two information obtained in this prodedure for the muon identification:

- Range of the associated KLM hits. The difference between measured and expected ranges is used as the discriminant.
- Goodness of the matching between the position of the associated KLM hits and that obtained by extrapolating the CDC track.

A likelihood ratio of the muon hypothesis and the pion hypothesis is made combining these two information and is used to separate muons from hadrons. Fig. 3.9 shows the muon detection efficiency versus momentum for an appropriate likelihood cut. For momentum between 1 GeV/c and 3 GeV/c, we have a muon identification efficiency of 89% with kaon and pion fake rate less than 2%.

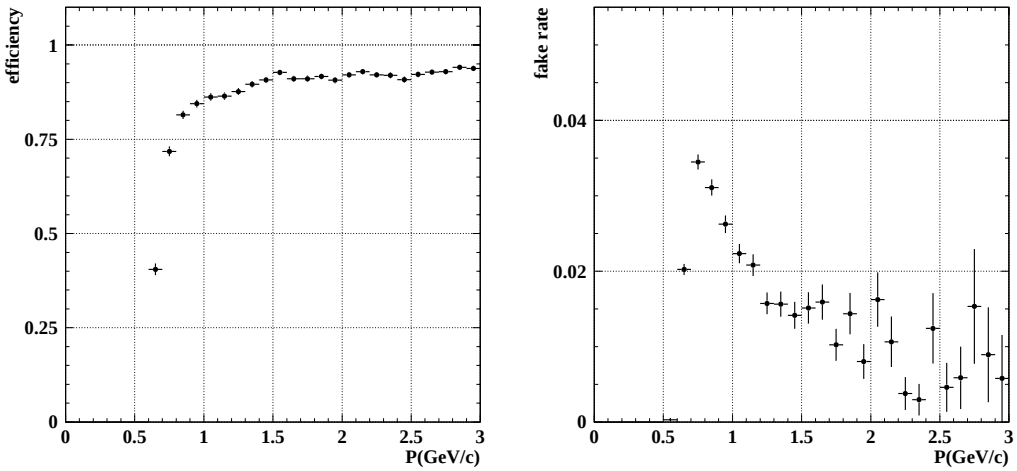

Figure 3.9: Muon detection efficiency (left) and fake rate (right) as a function of particle momenta.

3.2 Data Sample

In this analysis, a data sample collected by the end of 2006 at Belle detector at KEKB, a e^+e^- storage ring, are used. This data set consists of 605fb^{-1} taken at the $\Upsilon(4S)$ resonance state, which corresponds to 657 million $B\bar{B}$ pairs. The data is filtered by requiring the hadronic event selection.

3.2.1 Hadronic Event Selection

The data sample contains not only $\Upsilon(4S)$ events but also other processes: continuum $e^+e^- \to u\bar{u}, d\bar{d}, s\bar{s}, c\bar{c}, e^+e^- \to l^+l^-$, and two photon processes. It also contains cosmic ray events and beam background. To select the hadronic continuum and $B\bar{B}$ events, the following requirements are applied:

- At least three "good" tracks are found that come from the interaction point. Here, a "good" track has $p_t > 0.1$ GeV/c, $|\Delta r|$ <2cm and $|\Delta z| <$ 4cm, where $|\Delta r|$ and Δz are the closest distance of the track to the z-axis and the z coordinate of this closest point, respectively. p_t is the momentum projected on the xy-plane in the $\Upsilon(4S)$ rest frame. At this stage, a pion mass hypothesis is used for all charged tracks.

- More than one "good" cluster has to be measured in the barrel region ($-0.7 <$ cos$\theta < 0.9$) of the ECL, where a "good" cluster has an energy deposit of greater than 0.1 GeV in the $\Upsilon(4S)$ rest frame.

- The total visible energy (defined as the scalar sum of "good" tracks' momenta and sum of "good" cluster energies in the $\Upsilon(4S)$ rest frame), $E_{\rm vis}$, should exceed 20% of the center-of-mass energy.

- After boosting back to $\Upsilon(4S)$ rest frame with the assumption of being a massless particle, the sum of all cluster energies, $E_{\rm sum}$, should be between 0.1 and 0.8 of the center-of-mass energy.

- The sum of the absolute values of the z-component of all charged track momenta, $|p_z|$, and cluster energies, $|E\cos\theta|$, in the center-of-mass frame should be less than 50% of the total center-of-mass energy.

- The position of the primary vertex is required to satisfy $|r_{\rm vtx}| < 1.5$cm and $|z_{\rm vtx}| < 3.5$ cm, where primary vertex is obtained from all good charged tracks, r and z represent the position of the primary vertex in the r-ϕ plane and the z-axis, respectively.

The efficiencies of the hadronic event selection is 99.1% for $B\bar{B}$ events and 79.5% for continuum process, while the contamination of the non-hadronic components is less than 5%.[36]

3.3 Monte Carlo Method

The collected data by the Belle detector are analyzed at the offline computer system. The raw data are processed by reconstruction tools. The momentum, energy and particle ID information of each events are stored in tables to make the analysis easier for researchers. To make the analysis more reliable and more precise, a large amount of Monte Carlo (MC) simulation data is needed. In this section, we give introduction to the Monte Carlo datasets.

3.3.1 Event Generator

In this analysis, we choose the EvtGen [37, 38] software package as the event generator. This software package can simulate the physical process of particle decay chain. The decay table can be changed to control decays. Users can choose the proper decay properties (particle type, branching ratio, polarization state *et al.*) by changing the parameters of the decay table. The final state procuced by the generator will enter the detector simulation.

3.3.2 Detector Simulation

The full detector simulator GSIM is based on the GEANT3 [39] program, which is a large library program developed to simulate reactions between particles and matters. Data from EvtGen are input to GSIM which traces the behavior of each particle in the detector and simulate the detector response. The simulated events are reconstructed and analyzed with the same procedure as for real data.

3.3.3 Monte Carlo Data sample

In the analysis of the decay mode $B \to J/\psi\phi$, we use two kinds of Monte Carlo data sample: signal Monte Carlo and J/ψ inclusive Monte Carloto.

Signal Monte Carlo

To get the reconstruction efficiency for $B^0 \to J/\psi\phi$, we generate signal Monte Carlo events, which mean one of the $B^0\overline{B^0}$ decays into $J/\psi[\to l^+l^-]\phi[\to K^+K^-]$ and other B decays in "generic modes" (according to decay table including all known (or estimated) branching fractions). The decay type is set to SVV_HELAMP. Since the polarization direction and the detector configuration have a tight correlation with the detection efficiency, we generate these events with different properties separately. Table. 3.1 shows the summay of the singal Monte Carlo events.

	$J/\psi \to e^+e^-$	$J/\psi \to \mu^+\mu^-$
Transverse polarization in SVD1	50000	50000
Longitudinal polarization in SVD1	50000	50000
Transverse polarization in SVD2	50000	50000
Longitudinal polarization in SVD2	50000	50000

Table 3.1: Numbers of signal Monte Carlo events with different properties

Inclusive J/ψ Monte Carlo

The background estimation and the modeling of PDFs for final fit are based on the inclusive J/ψ Monte Carlo. The inclusive J/ψ Monte Carlo is to simulate the $B\bar{B}$ events in which one B meson decays through one of decay among all known decay modes including J/ψ in final state (either directly from B or secondary such as $\psi' \to J/\psi\pi\pi, \chi_{c1} \to J/\psi\gamma$ etc.) and the other B decays generically. The amount of the sumulated events is equivalent to 3.88 $\times 10^{10} B\bar{B}$.

3.4 Reconstruction of $B^0 \to J/\psi\phi$

In this analysis, the final state we used to reconstruct meson J/ψ is lepton pairs and that of meson ϕ is charged kaon pairs.

To suppress the contimuum ($e^+e^- \to q\bar{q}$, where $q = u, d, s, c$) background, the events are required to satisfy $R_2 < 0.5$, where R_2 is the ratio of the second to zero-th Fox-Wolfram moments [41].

The charged tracks are required to have $|dz| < 5$ cm and $|dr| < 0.3$ cm, where dr and dz are the impact parameters defined by the event-dependent interaction point (IP). This requirement is introduced to eliminate the wrongly reconstructed tracks.

3.4.1 Reconstruction of J/ψ candidate

The reconstruction of J/ψ is performed using its decays into two charged lepton pairs.

J/ψ candidates are selected by the invariant mass cut. To reduce the effect of bremsstrahlung or final state radiation, clusters in the calorimeter within 50 mrad from the electron's(or positron's) initial momentum vector are included to calculate the invariant mass The requirements for candidates of J/ψ are $-0.15 < (M_{ee(\gamma)} - m_{J/\psi}) < 0.036$ GeV/c^2 and $-0.06 < (M_{\mu\mu} - m_{J/\psi}) < 0.036$ Gev/c^2 for e^+e^- and $\mu^+\mu^-$ modes respectively, where $m_{J/\psi}$ denotes the world average of the J/ψ mass. The mass cut is asymmetric because of the radiative tails. The invariant mass distributions of lepton pairs are shown in Fig. 3.10.

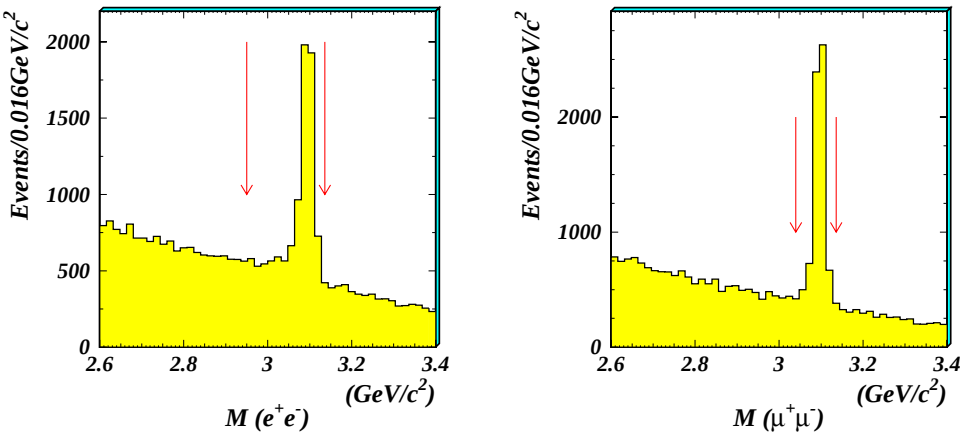

(a) Mass distribution of e^+e^- (γ). (b) Mass distribution of $\mu^+\mu^-$.

Figure 3.10: The mass distribution of $J/\psi \to l^+l^-$. The red arrows show the selected mass regions.

To improve the momentum resolution, we apply vertex fit and mass constrained fit for J/ψ candidates that passed the above selection criteria.

3.4.2 Reconstruction of ϕ candidate

The reconstruction of ϕ meson is performed using its decays into two charged kaon pairs. We require the $\mathcal{R}(K : \pi) > 0.7$ to separate kaons from pions, which has a efficiency for kaon-pion separation of 90 % and a 5.9 % probability to misidentify a pion as kaon. The requirements for candidates of ϕ are $-0.01 < (M_{KK} - m_\phi) < 0.01$ GeV/c^2, where m_ϕ denotes the world average of the ϕ mass [13]. The invariant mass distribution of kaon pairs is shown in Fig. 3.11.

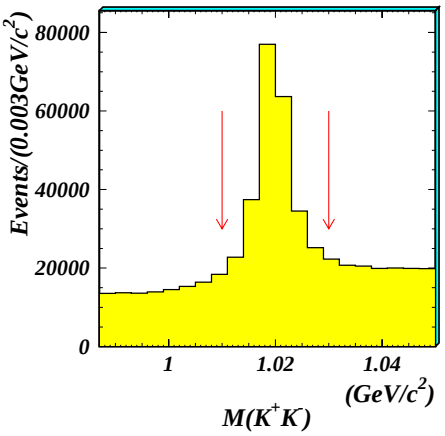

Figure 3.11: The mass distribution of $\phi \to K^+K^-$. The red arrows show the selected mass region.

3.4.3 Reconstruction of B candidate

Reconstruction of B mesons is done by combining J/ψ candidates and ϕ candidates. We use two kinematic variables: energy difference ΔE, and beam constrained mass $M_{\rm bc}$ to isolate B candidates from background.

$$M_{\rm bc} = \sqrt{E^2_{\rm beam} - P^2_B}, \tag{3.12}$$

$$\Delta E = E_B - E_{\rm beam}. \tag{3.13}$$

Here, P_B is the center-of-mass (c.m) momentum of the reconstructed B meson,E_B is the c.m energy of the reconstructed B meson, and $E_{\rm beam}$ is the c.m beam energy. The $E_{\rm beam}$ is measured using $B^+ \to D^{(*)0}\pi^+$ sample in run-by-run basis.

The $M_{\rm bc}$, ΔE and $M_{\rm bc}$-ΔE 2D distributions from signal Monte Carlo are shown in Fig. 3.12. The $M_{\rm bc}$ distribution peaks at B mass with the resolution $\sigma \sim 3$ MeV/c^2 which is dominated by beam energy spread. The ΔE distribution peaks at zero and its resolution is due to track momentum resolution: $\sigma \sim 6$ MeV with small wider tail component.

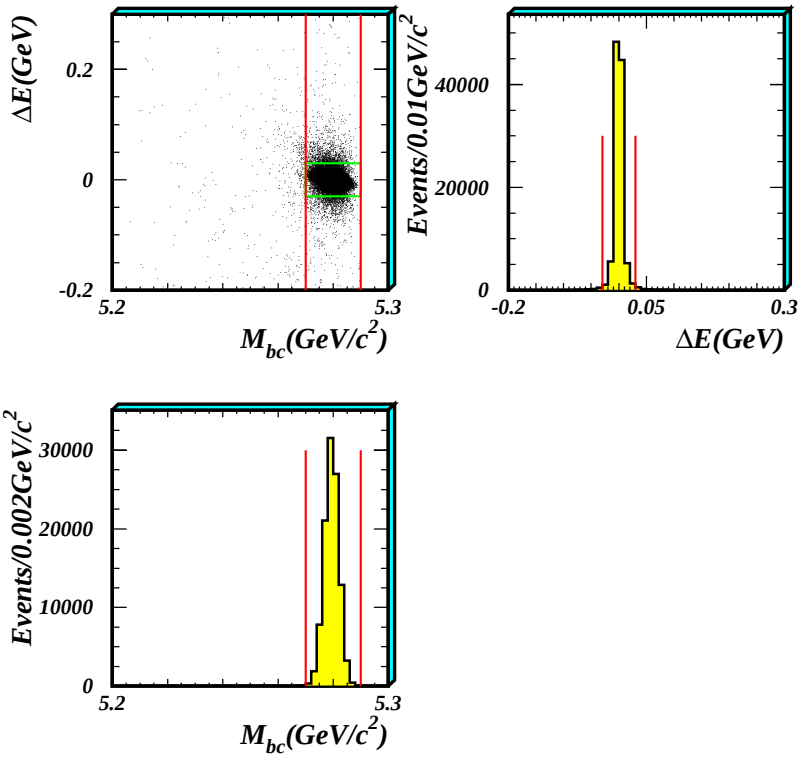

Figure 3.12: Upper left: $M_{\rm bc}$-ΔE 2D distribution for $B \to \psi\phi$ signal Monte Carlo 400,000 events with $B^0 \to \psi\phi$ selection being applied. Upper right: ΔE projection in 5.27 GeV/c^2 $< M_{\rm bc} <$ 5.29 GeV/c^2. Lower: $M_{\rm bc}$ projection in -0.03 GeV $< \Delta E <$ 0.03 GeV. Red and green lines show the selected regions metioned above.

3.4.4 Best B candidate selection

We check the number of B candidates in a event using $B \to J/\psi\phi$ signal MC sample. We find about 4.9% of the events have multiple B candidates (number of B candidates is $\geq$2). These multiple candidates mostly consist of multiple ϕ candidates with a common J/ψ candidate. To keep only one B candidate per event, We choose the B candidate whose daughter particle ϕ has the most closest mass to the nominal ϕ mass [13].

Chapter 4

Signal Yield Extraction

In this chapter, we will introduce the signal yield extraction. We analyze the soure of the peaking background, then based on the analysis we choose the proper probability density function (PDF) to establish the maximum-likelihood function, finally we determine the parameters of the PDFs using the information from MC and data sample.

4.1 Background

The dominant background comes from $B\bar{B}$ events with B decays to J/ψ. We study the background using the J/ψ inclusive Monte Carlo data sample corresponding to $3.88 \times 10^6 B\bar{B}$ events (about 59 times the data sample). The J/ψ inclusive Monte Carlo is to simulate the $B\bar{B}$ events in which one B decays to final states including a J/ψ meson. The selection result of J/ψ inclusive Monte Carlo sample is shown in Fig. 4.1.

As seen in Fig. 4.1, there are two peaking-background components in (ΔE, $M_{\rm bc}$) distribution: one is $B^0 \to J/\psi K^{*0}(K^{*0} \to K^+\pi^-)$ and the other is $B^{0/-} \to J/\psi K_1(1270)$. Both have a peak in the signal region of $M_{\rm bc}$ ($5.27{\rm GeV}/c^2 < M_{\rm bc} < 5.29{\rm GeV}/c^2$), but different peak structures in ΔE distribution as shown in Fig. 4.2.

We explain why those two kinds of backgrounds peak in ΔE signal region as the following:

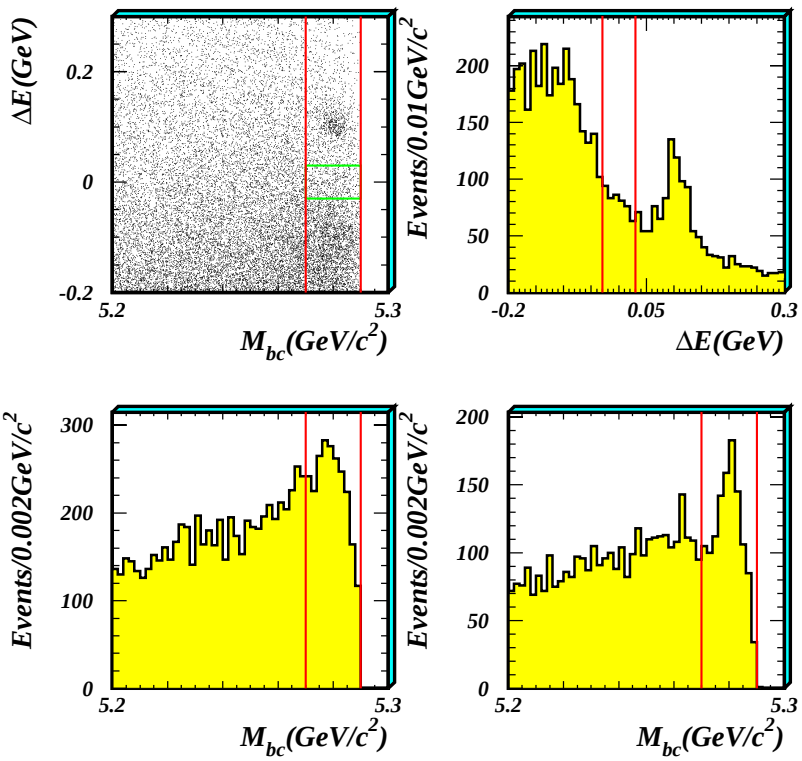

Figure 4.1: Upper left: $M_{\rm bc}$-ΔE 2D distribution for J/ψ inclusive Monte Carlo 3.88×10^6 events with $B^0 \to J/\psi\phi$ selection being applied. Upper right: ΔE projection in 5.27 GeV/c^2 $< M_{\rm bc} <$ 5.29 GeV/c^2. Lower left: $M_{\rm bc}$ projection in -0.15 GeV $< \Delta E < 0$ GeV ($J/\psi K_1$ peaking region). Lower right: $M_{\rm bc}$ projection in 0 GeV $< \Delta E <$ 0.15 GeV ($J/\psi K^{*0}$ peaking region). Red and green lines show the selected regions mentioned above.

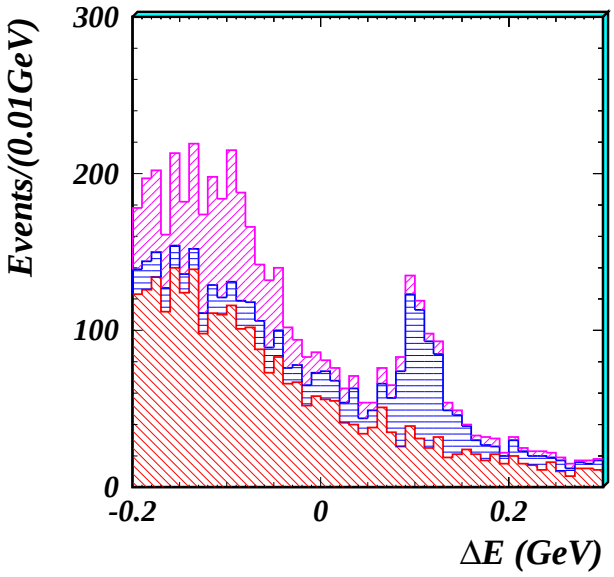

Figure 4.2: ΔE distribution of J/ψ inclusive MC ($5.27 < M_{\rm bc} < 5.29$ GeV/c^2).

- $B^0 \to J/\psi K^{*0}$ mode: In this case, $K^{*0}(892) \to K^+\pi^-$, then one pion is mis-identified as kaon, this fake kaon combined with the real kaon makes one $\phi(1020)$ meson candidate. This process will make a peak at $\Delta E \sim 0.1$ GeV.

- $B^{0/-} \to J/\psi K_1(1270)$ mode: In this case, $K_1(1270)$ decay to the final states including $J/\psi, K^-, \pi^+, \pi^{0/-}$. If one pion is mis-identified as kaon and the other pion is not used, the fake kaon and the real kaon can make a ϕ meson candidate. This process will make a peak in the negative ΔE region.

The remaining background (red part of Fig. 4.2) is due to random combinations of J/ψ and ϕ candidates and does not peak in the ΔE distribution (referred to as combinatorial background).

4.2 Unbinned Extended Maximum Likelihood Fit

Since there is no background component peaking at the signal region in ΔE distribution and we know well the properties of the two main peaking background components, we extract the signal yields by performing a one dimensional (1D) unbinned extended maximum-likelihood fit to the ΔE distribution candidate events. The likelihood function is

$$\mathcal{L} = \frac{e^{-\sum_k N_k}}{N!} \prod_{i=1}^{N} \left[\sum_k N_k \times P_k(\Delta E^i) \right],$$

where N is the total number of candidate events, i is the identifier of the i-th event, N_k and P_k are the yield and probability density function (PDF) of the component k, which corresponds to the signal, $B \to J/\psi K_1$, $B^0 \to J/\psi K^{*0}$, and combinatorial backgrounds.

4.2.1 Background PDFs

The PDFs of combinatoric background and K_1 components for final fit are coming from the fit of J/ψ inclusive MC sample(Fig. 4.3 and Fig. 4.5). For combinatoric background, we get the parameters of the PDF from the fit to J/ψ inclusive MC sample. The sample contains only the combinatoric background component. We use the 2nd order Chebychev polynomial function to fit this MC sample, the fit result is shown in Fig. 4.3.

To verify that the MC sample describe the real data well enough, we fit the J/ψ inclusive MC sample and data sample in $M_{\rm bc}$ & M_{KK} sideband using the 2nd order Chebychev polynomial and compare the results. The $M_{\rm bc}$ sideband region is defined as $(5.22-5.26)\mathrm{GeV}/c^2$ and the M_{KK} sideband is defined as $(1.04-1.10)\mathrm{GeV}/c^2$. We draw the MC and data curves together in Fig. 4.4. We can see that two curves are quite close, which means we can safely use the PDF from MC to fit the real data.

The parameters of the $B \to J/\psi K_1$ PDF are obtained from the fit to events containing $B \to J/\psi K_1(1270)$ in the J/ψ inclusive data sample. The sample contains both peaking and combinatoric background components. The PDF is the sum of two Gaussian functions. We fix the shape of combinatoric background component to the

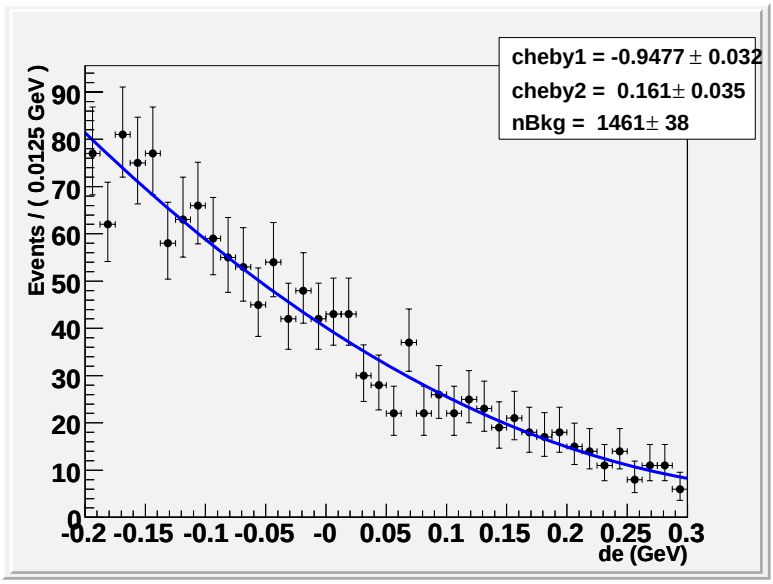

Figure 4.3: PDF of combinatoric background for final fit

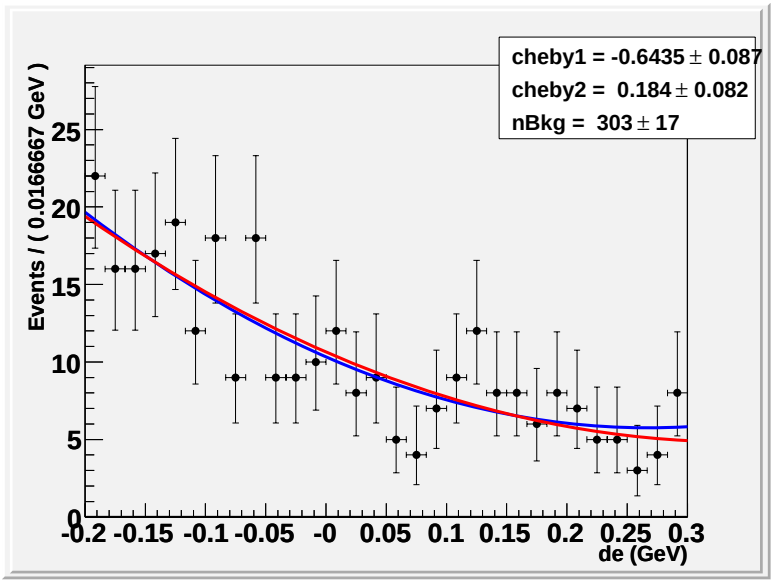

Figure 4.4: Comparation of data and MC shape in $M_{\rm bc}$ & M_{KK} region. The points with errors are the data. The red curve represents scaled MC shape, the blue curve is a fit to the data.

one obtained above and float its yield. We also let free the shape parameters and yield of the peaking component (called K_1 PDF). To get the shape parameters more precisely, we extend the fit region to -0.28 Gev. The fit result is shown in Fig. 4.5.

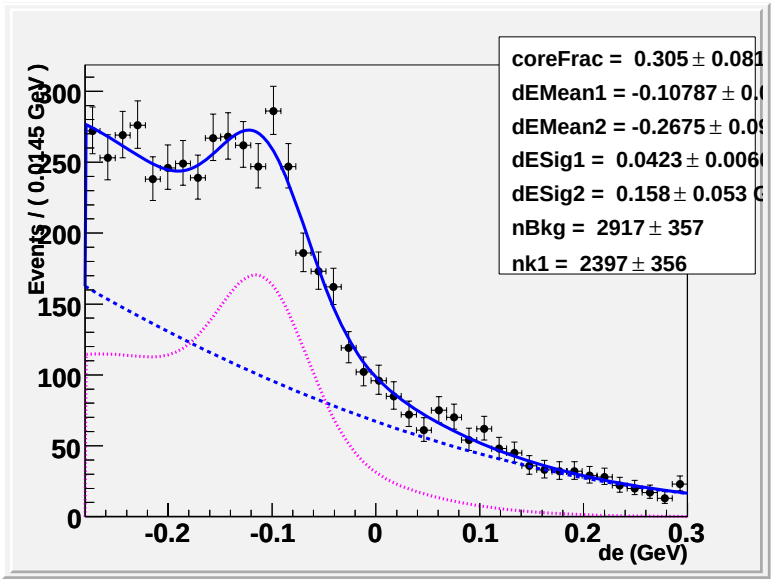

Figure 4.5: PDF of $B \to J/\psi K_1$ component for final fit using J/ψ inclusive MC. The red dotted curve is K_1 PDF and the blue dashed curve is combinatorial component.

The PDF of $B^0 \to J/\psi K^{*0}$ component is obtained from the fit to the $B^0 \to J/\psi K^{*0}$ MC sample. This MC sample has a higher statistics (300,000 events) than $B^0 \to J/\psi K^{*0}$ events in the inclusive J/ψ MC. The PDF is bifuscated Gaussian function. The fit result is shown in Fig. 4.6.

At last we apply the PDFs to the J/ψ inclusive MC sample to check whether the fit is valid. The fit result is shown in Fig. 4.7.

4.2.2 Signal PDF

The signal PDF is modeled by a sum of two Gaussians with a common mean value. The parameters of the PDF come from the fit to the signal MC sample, however, there could be some differences between MC and data. To take them into account,

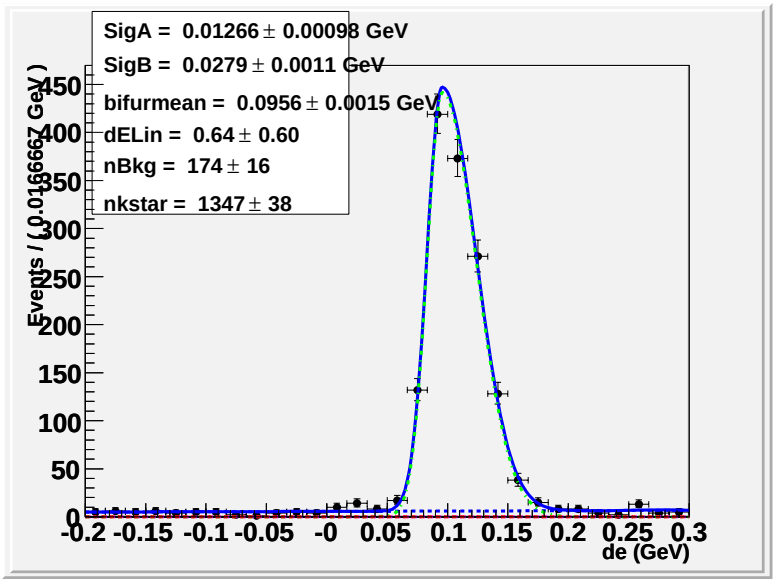

Figure 4.6: PDF of K^{*0} for final fit using $J/\psi K^{*0}$ signal MC

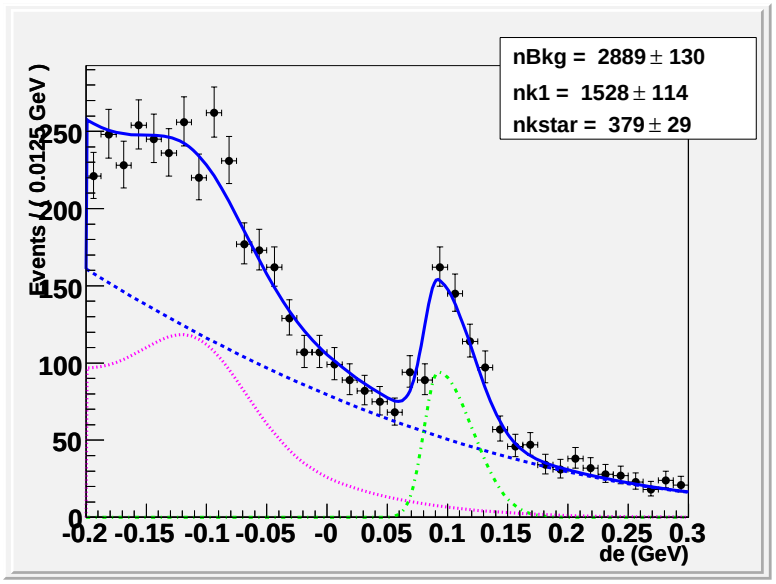

Figure 4.7: Fit result to J/ψ inclusive MC sample, with all background components included.

we compare MC and data results of $B^0 \to J/\psi K^{*0}[K^{*0} \to K^-\pi^+]$ mode to evaluate the fudge factors: mean shift and resolution difference between data and MC. The $B^0 \to J/\psi K^{*0}$ events are selected with the same selection criteria except that a pion is required $\mathcal{R}(K/\pi) < 0.6$ instead of $\mathcal{R}(K/\pi) > 0.7$ for one of two tracks and $|M_{K\pi} - m_{K^{*0}}| < 0.075$ GeV/c^2 are required.

From the Fig. 4.8, we can see that the peak position of the signal in data(right figure) is shifted to the left and the resolution is broader than the one in MC(left figure).

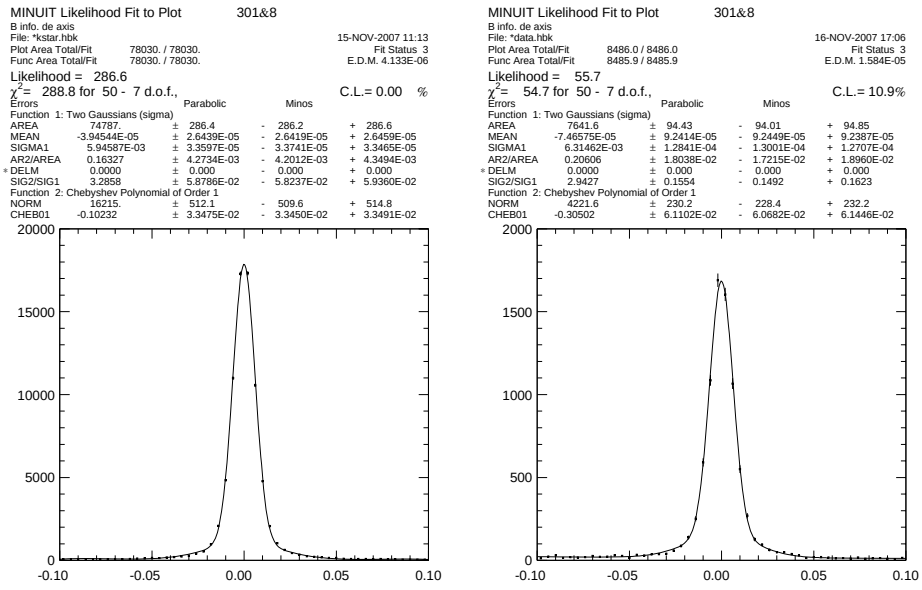

Figure 4.8: ΔE distribution for the $B \to J/\psi K^{*0}$ in MC(left) and data(right). The fit is described in the test.

We first fit the MC sample. Then, we fit the data with a ratio of the areas of two Gaussians ("Ar2/AREA") fixed to that obtained from MC sample. The fudge factor of "MEAN" is the difference of the "MEAN" value in MC and data; the fudge factor of "SIGMA1" is the ratio of "SIGMA" value in data over that in MC. These factors are shown in Table. 4.1. For $B^0 \to J/\psi\phi$, we generate signal MC sample with mixture of 50% transversely polarized and 50% longitudinaly polarized events. The

fit result and the corrected signal PDF parameters for final fit are shown in Fig. 4.9 and Table. 4.2.

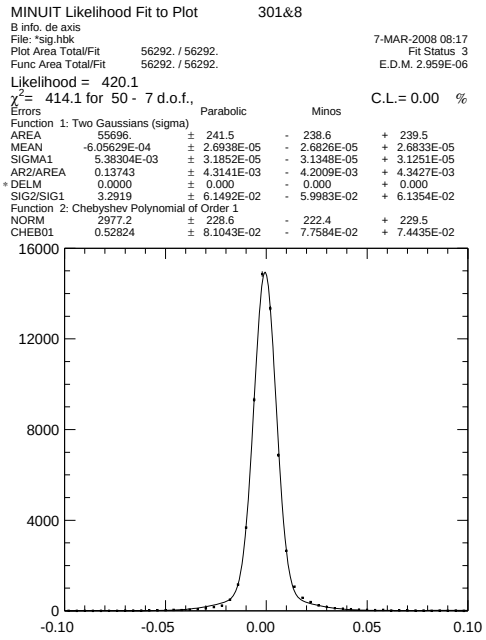

Figure 4.9: PDF of $J/\psi\phi$ signal

	MEAN(MeV)	SIGMA1(MeV)	SIGMA2/SIGMA1
MC	-0.182 ± 0.025	5.835 ± 0.022	3.092 ± 0.040
data	-0.075 ± 0.093	6.547 ± 0.082	3.167 ± 0.151
fudge factor	0.107 ± 0.096	1.122 ± 0.015	1.024 ± 0.050

Table 4.1: Fudge factor estimation using $B^0 \to J/\psi K^{*0}$ control sample.

	MEAN(MeV)	SIGMA1(MeV)	SIGMA2/SIGMA1
MC($B \to J/\psi\phi$)	-0.606 ± 0.027	5.383 ± 0.032	3.292 ± 0.062
fudge factor	0.107 ± 0.096	1.122 ± 0.015	1.024 ± 0.050
Corrected Parameters	-0.499 ± 0.100	6.040 ± 0.091	3.371 ± 0.175

Table 4.2: PDF parameters for final fit (before and after correction)

Chapter 5

Results

In this chapter, we will give the results of this analysis. We will firstly give the fit result of the data sample, then we describe how to estimate the systematic uncertainty, finally we evaluate the upper limit of the signal yield and the corresponding branching fraction.

5.1 Fit Result

The reconstruction result of whole data sample is shown in Fig. 5.1.

In the final fit, the yields of the $J/\psi K^{*0}$, $J/\psi K_1(1270)$, combinatorial background and signal components are free and the shape parameters of the PDFs of all the components are fixed. The fit is applied to 85 candidates in ΔE distribution. The fit result is shown in Fig. 5.2. We obtain a signal yield of $4.6^{+3.2}_{-2.5}$ events with a statistical significance of 2.3σ. This statistical significance is defined as $\sqrt{-2\ln(\mathcal{L}_0/\mathcal{L}_{\rm max})}$, where $\mathcal{L}_{\rm max}$ and $\mathcal{L}_0$ denote the maximum likelihood with the fitted signal yield and with the yield fixed to zero, respectively.

Table. 5.1 gives the yield of each component. The number of misidentified $B^0 \to J/\psi K^{*0}$ events obtained from the fit is $22.5\ ^{+5.4}_{-4.8}$ and is consistent with the expectation 12.6 ± 0.9 obtained from MC simulation incorporating the misidentification probability and the world average branching fraction [13].

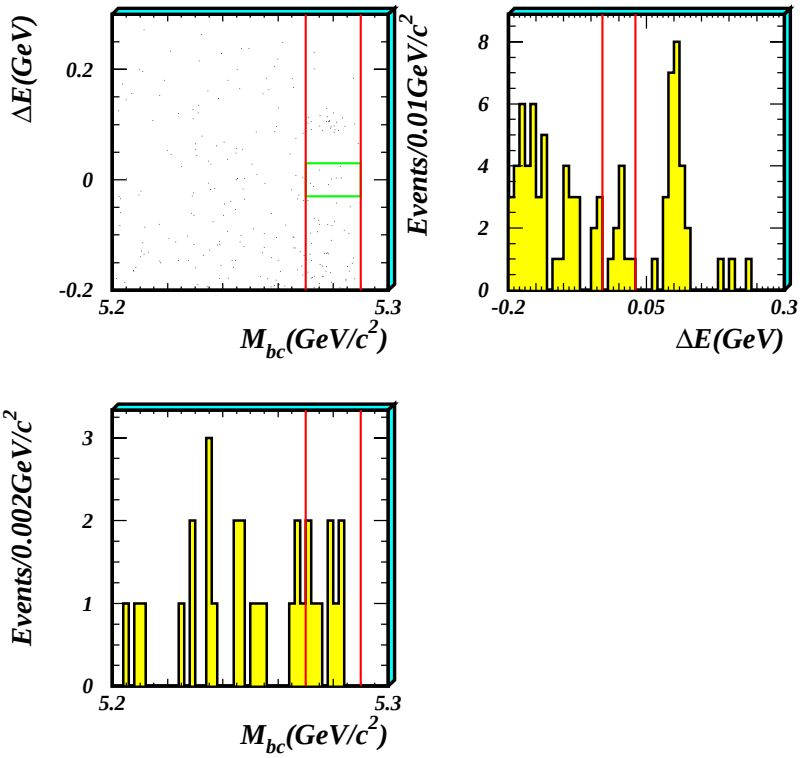

Figure 5.1: Upper left: $M_{\rm bc}$-ΔE 2D distribution for real data with $B^0 \to \psi\phi$ selection being applied. Upper right: ΔE projection in 5.27 GeV/c^2 $< M_{\rm bc} <$ 5.29 GeV/c^2. Lower: $M_{\rm bc}$ projection in -0.03 GeV $< \Delta E <$ 0.03 GeV. Red and green lines show the selected regions mentioned above.

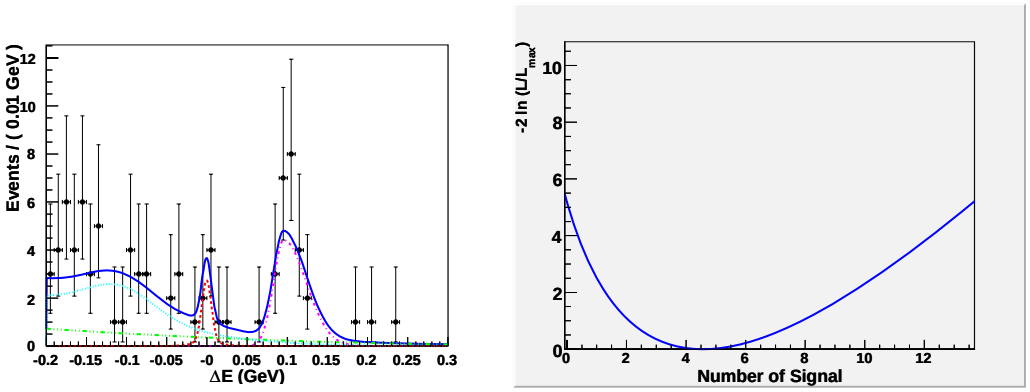

Figure 5.2: Results of the final fit Left:ΔE distribution for the decay $B \to J/\psi\phi$. The curves show the signal (red dashed lines) and the background (cyan dashed lines for $J/\psi K_1$ component, magenta dashed lines for $J/\psi K^{*0}$ component and green triple-dot dashed lines for combinatorial backgrounds) contributions as well as the overall fit (blue solid lines).Right: Log likelihood ratio curve.

Component	Yield (central value)	+ MINOS error	− MINOS error
Signal	4.6	3.2	−2.5
$J/\psi K^{*0}$	22.5	5.4	−4.8
$J/\psi K_1(1270)$	41.7	11.3	−12.4
Combinatorical Background	16.3	13.7	−9.7

Table 5.1: Final fit result.

5.2 Branching Fraction Calculation

The branching fraction is given with

$$\mathcal{B}(B^0 \to J/\psi\phi) = N_S/[\epsilon \times N_{B\bar{B}} \times \mathcal{B}(J/\psi \to l^+l^-) \times \mathcal{B}(\phi \to K^+K^-)] \qquad (5.1)$$

Where N_S is the signal yield and $N_{B\bar{B}}$ is the number of $B\bar{B}$ pairs. The fractions of neutral and charged B mesons produced in $\Upsilon(4S)$ decays are assumed to be equal. We use the world averages [13] for the branching fractions of $\mathcal{B}(J/\psi \to l^+l^-)$ and $\mathcal{B}(\phi \to K^+K^-)$.

The efficiency (ϵ) is determined from the signal MC sample with the same selection

as used in the data and the correction is applied to take account the difference between data and MC simulation. We use $B^0 \to J/\psi\phi$ signal MC events with a mixture of 50% transverse and 50% longitudinal polarizations to determine the nominal efficiency. Since the selection efficiency depends on the two detector configurations (SVD1 and SVD2 as described in Sec.2.2), we obtain the efficiency for each configuration and take a weighted average according to the number of $B\bar{B}$ events of two configurations. We have checked possible efficiency differences between the data and MC simulation in each selection criterion using various calibration samples. The MC efficiencies agree well with the data, except for the muon-ID efficiency. We correct the MC efficiency due to this difference and obtain 26.2%. The details of the efficiency calculations together with systematic errors are described in the next section.

5.3 Systematic Uncertainties

The sources of systematic errors are divided into two large categories: systematic error in reconstruction efficiency and systematic uncertainty in signal extraction.

5.3.1 Systematic Error in Reconstruction Efficiency

- **Tracking Efficiency Error**.

  The systematics due to the tracking efficiency uncertainty [42] is obtained by comparing the efficiencies for data and MC using the D^*-tagged $D^0 \to K^0_S\pi^+\pi^-$ sample. The decay chain is reconstructed without using one of pions from K^0_S and the tracking efficiency of the pion can be examined. Because the charged particles of kaons and leptons behave similar with charged pions, we can use the same tracking efficiency error. We get the error of 1.05% for each track. The total systematic error from tracking efficiency is then 4.2%.

- **Kaon ID Efficiency Error**

  The systematic error of kaon identification [43, 44]are studied by comparing the MC sample and data sample of decay mode $D^{*+} \to D^0\pi^+$ followed by $D^0 \to K^-\pi^+$ as described in Sec. 3.1.1. We get the error of 1.1% for each kaon. The total systematic error due to kaon ID efficiency is then 2.2%.

- **Lepton ID Efficiency Error**

  We use control samples of $J/\psi \to \ell^+\ell^-$ and $e^+e^- \to e^+e^-\ell^+\ell^-$ events to estimate lepton identification efficiency corrections and uncertainties [45]. For the $J/\psi \to \mu^+\mu^-$ mode, the correction factors are obtained for SVD1 and SVD2 separately and the average efficiency is calculated with a weights of number of $B\bar{B}$ and raw MC efficiencies. Using the values of Table 5.2, we find the efficiency for a muon track in the data to be (4.3 ± 3.1)% lower than that of MC simulation. We correct the efficiency for this difference and assign a 3.1% uncertainty per muon track. For the $J/\psi \to e^+e^-$ mode, the difference between

efficiencies in the data and in the MC simulation is small, and we assign a 2.7% uncertainty per electron track based on their difference and errors.

	SVD1	SVD2
Raw MC Efficiency(e)	24.4%	26.7%
Raw MC Efficiency(μ)	27.4%	29.0%
Correction for a muon	0.971 ± 0.023	0.953 ± 0.031
Correction for $J/\psi \to \mu^+\mu^-$	0.9428	0.9082

Table 5.2: Raw MC efficiencies and corrections due to muon ID

Corrected Efficiency	$0.5 * (0.23 * 0.244 + 0.77 * 0.267)$
	$+0.5 * (0.23 * 0.274 * 0.943 + 0.77 * 0.29 * 0.908) = 26.2\%$
Sys.Error due	$SQRT((0.5 * (0.23 * 0.244 + 0.77 * 0.267) * 0.054)^2$
to Lepton ID	$+(0.5 * (0.23 * 0.274 * 0.943 + 0.77 * 0.29 * 0.908) * 0.062)^2) = 0.011$

Table 5.3: Calculations of corrected efficiency and systematic error due to Lepton ID

The combined efficiency for $J/\psi \to \mu^+\mu^-$ and $J/\psi \to e^+e^-$ modes is calculated as shown in Table 5.3, The corrected reconstruction efficiency is 26.2 %. The systematic error due to Lepton ID is $\pm$ 0.011 (*i.e.* 4.2 % of the corrected efficiency).

- **Polarization**

  To get the systematic error due to the unknown polarization, we consider two extreme situations: totally transverse polarization and totally longitudinal polarization. The raw MC efficiencies (since only relative efficiency difference is needed, the muon-ID correction is not applied here) in these extreme situations are listed in Table 5.4.

  The difference from the average of two cases ($\pm$2.6 % including the statistical errors of the MC samples) is assigned as systematic error.

- **Secondary Branching Fraction**

	Transverse	Longitudinal
SVD1	25.4 ± 0.2	26.3 ± 0.2
SVD2	27.1 ± 0.2	28.6 ± 0.2
Average	26.7 ± 0.2	28.1 ± 0.2

Table 5.4: Raw MC efficiencies for different polarizations

We use the secondary branching ratio of $J/\psi \to l^+l^-$ and $\phi \to K^+K^-$ to estimate the branching ratio, it will also introduce some systematic error. We use the value of PDG 2006 [13]. ($J/\psi \to l^+l^-$: $(11.87 \pm 0.08)\%$, $\phi \to K^+K^-$: $(49.2 \pm 0.6)\%$).

- **Number of $B\bar{B}$**

  The systematic error about the number of $B\bar{B}$ events is obtained from the official number of $B\bar{B}$ pairs, $(657 \pm 9) \times 10^6$

Tabel. 5.5 summarizes these systematic errors.

Uncertainty Source	$\Delta\varepsilon(\%)$
Tracking efficiency	4.2
Lepton ID efficiency	4.2
Polarization	2.6
Kaon ID efficiency	2.2
Number of $B\bar{B}$	1.4
ϕ branching fraction	1.2
J/ψ branching fractions	0.7
Total	7.2

Table 5.5: Summary of systematic uncertainties (%) other than signal yield extraction.

Uncertainty Source	Shape Parameter	$(+\sigma)\Delta n$	$(-\sigma)\Delta n$
Signal	MEAN	< 0.1	< 0.1
	SIGMA1	< 0.1	0.1
	SIGMA2	< 0.1	< 0.1
	Core Fraction	< 0.1	< 0.1
K_1	MEAN1	0.2	< 0.1
	MEAN2	0.8	0.5
	SIGMA1	0.2	< 0.1
	SIGMA2	0.5	1.1
	Core Fraction	< 0.1	0.2
K^{*0}	MEAN	< 0.1	< 0.1
	SIGMA1	< 0.1	< 0.1
	SIGMA2	< 0.1	< 0.1
Background	CHEB1	(+15%) 0.1	(-15%) 0.2
	CHEB2	(+30%) < 0.1	(-30%) 0.1
Total		1.0	1.2

Table 5.6: Systematic uncertainty in the signal extraction

5.3.2 Systematic Error in Signal Yield Extraction

The uncertainty in the yield extraction from the fit is determined by varying the parameters of PDFs by $\pm 1\sigma$ of the measured errors (the errors are given in Sec. 4.2.1). For the combinatorial background, we vary $\pm 15\%$ for the first order coefficient and $\pm 30\%$ for the second order coefficient. The result is shown in Table 5.6. The dominant uncertainty is coming from the $J/\psi K_1(1270)$ component.

Finally, the total systematic error is 27.1%.

5.4 Upper Limit Estimation

As no significant signal is found for the $B^0 \to J/\psi\phi$ decay mode, we obtain an upper limit on the yield at the 90% confidence level (Y_{90}) by a frequentist method using ensembles of pseudo-experiments (Toy MC). The Toy MC samples are generated with the same PDFs as we used for final fit. The number of background events in each

component is generated according to Poission distribution with mean value obtained by the fit to the data. We generate several Toy MC ensembles with 10,000 sets for different mean value of the signal yield. We then fit each Toy MC sample using the same method as for the final fit for the real data. For an ensemble with given mean signal yield, the fraction that the fit signal yield is greater than 4.6 is taken as a confidence level. We account for systematic error by randomly smearing the fit yield by a Gaussian distribution with the width of the total systematic error. Fig. 5.3 showes an example of the distributions of the fit yield. Fig. 5.4. shows the confidence level as a function of the (mean) signal yield.

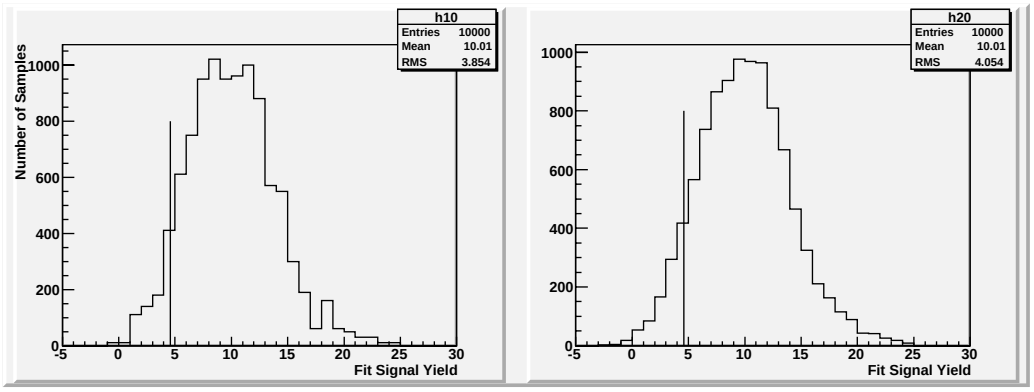

Figure 5.3: Distribution for fit signal yield (input mean signal yield 10), left: without systematic error smeared; right: with systematc error smeared.

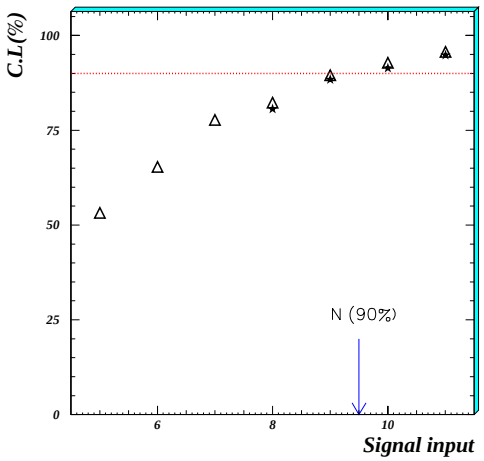

Figure 5.4: The confidence level as a function of the (mean) signal yield.

Mode	Y	Sig.	n_0	Y_{90}	$\epsilon(\%)$	$\mathcal{B}$
$B \to J/\psi\phi$	$4.6^{+3.1}_{-2.5}$	2.3σ	85	9.5	26.2	$< 9.4 \times 10^{-7}$

Table 5.7: Summary of the results. Y is the signal yield from the fit, Sig. is the statistical significance, n_0 is the number of candidate events used in the fit, Y_{90} is the upper limit on the signal yield at 90% confidence level, ϵ is the detection efficiency and $\mathcal{B}$ is the upper limit of branching fraction at the 90% confidence level.

We obtain an upper limit on the signal yield at the 90% confidence level (Y_{90}) to be 9.5 by linearly interpolating the points around 90% line. Inserting this Y_{90} value in Eq. 5.1, we obtain the upper limit of branching fraction at the 90% confidence level:

$$\mathcal{B}(B^0 \to J/\psi\phi) < 9.4 \times \ 10^{-7}. \tag{5.2}$$

The result is summarized in Table. 5.7.

5.5 Validity Check with $B^0 \to J/\psi K^{*0}$

To check the validity of this analysis, we apply the same reconstruction method to the decay mode $B^0 \to J/\psi K^{*0}$. The $B^0 \to J/\psi K^{*0}$ events are selected with the same selection criteria except that a pion is required $\mathcal{R}(K/\pi) < 0.6$ instead of $\mathcal{R}(K/\pi) > 0.7$ for one of two tracks and $|M_{K\pi} - m_{K^{*0}}| < 0.075$ GeV/c^2 are required.

The reconstruction efficiency is 23.5% and the signal yield is 15219 ± 129. The calculated branching fraction is $(1.24 \pm 0.01) \times 10^{-3}$ (statistical error only), which is consistent with the world average value [13].

Chapter 6

Discussion and Summary

We have searched for the decay $B^0 \to J/\psi\phi$ and give an upper limit on the branching fraction at 90% confidence level:

$$\mathcal{B}(B^0 \to J/\psi\phi) < 9.4 \times\ 10^{-7}, \tag{6.1}$$

based on data sample of 657×10^6 $B\bar{B}$ pairs. Comparing with the previous result from BaBar collaboration

$$\mathcal{B}(B^0 \to J/\psi\phi) < 9.2 \times\ 10^{-6}, \tag{6.2}$$

this result has improved the upper limit of this decay mode almost by a factor of 10.

As discussed in Sec.1.3, the dominant mechanism that contributes to this decay mode is ω-ϕ mixing through $B^0 \to J/\psi\omega$ decay. According to the theoretical calculation, this contribution will lead to a branching fraction of about $(1.8 \pm 0.3) \times 10^{-7}$. Final State Interaction (rescattering effect) also contributes to this decay, its contribution is estimated about $\sim 10^{-8}$ with a large uncertainty. If $B^0 \to D_s^{(*)+} D_s^{(*)-}$ decays and the rescattering process are enhanced, its contribution my be $> 10^{-6}$. The contributions from other processes are estimated to be less than 10^{-11}.

Our result indicates that an large enhancement from the rescattering process is unlikely in this decay mode [19] and the upper limit is about five times larger than the theoretical prediction with ω-ϕ mixing contribution.

It should be noted that our result imposes the strigent limit on the contribution of $U(3)$ breaking component between $B_s \to J/\psi\phi$ and $B^0 \to J/\psi K^{*0}$ decays [46].

The ω-ϕ mixing contribution can be also studied with $B^0 \to D^{(*)0}\omega \to D^{(*)0}\phi$ and $B^+ \to \pi^+(\rho^+)\omega \to \pi^+(\rho^+)\phi$ decays [19]. These decay modes have been studied with only small data sample [47, 48, 49] and studies with fully available data sample would be interesting.

To get a better understand of this decay mode, a larger luminosity is needed. In order to measure the predicted branching fraction, about 25 times more data ($\sim$ 16 billion $B\overline{B}$ events) is needed, the signals could be observed with less data if moderate inhancement exists in rescattering process. In the future, the super B factory will accumulate up to 50 billion $B\overline{B}$ events. With such a large data sample, we can take a precise measurement and the result is surely useful to understand the ω-ϕ mixing and rescattering effect.

Bibliography

[1] S. L. Glashow, Nucl. Phys. 22 579-588 (1961); S. Weinberg, Phys. Rev. Lett. **19**, 1624 (1967); A. Salam, in Elementary Particle Theory, N. Svartholm ed., Almqvist and Wiksells, p. 367 (1968).

[2] C. Quigg, *Gauge Theories of the Strong, Weak and Electromagnetic Interactions* (Addison-Wesley, Boston, 1993).

[3] M. Kobayashi and T. Maskawa, Prog. Th. Phys. **49**, 652 (1973).

[4] L. Wolfenstein, Phys. Rev. Lett. **51**, 1945 (1983).

[5] L.D. Landau: Dokl. Akad. Nauk USSR **60**, 207 (1948); C.N. Yang: Phys. Rev. **77**, 242 (1950).

[6] G. Zwig, CERN Report No. 8419 TH 412, 1964 (unpublished); S. Okubo, Phys. Lett. **5**, 165 (1963); Phys. Rev. D **16**, 2336 (1977); J. Iizuka, K. Okada, and O. shito, Prog. Th. Phys. **35**, 1061 (1966); J. Iizuka, Prog. Th. Phys. Suppl. **37-38**, 21 (1966).

[7] C. W. Bauer, D. Pirjol, I. Z. Rothstein and I. W. Stewart, Phys. Rev. D **70**, 054015 (2004).

[8] Gong-ru Lu, Ru-min Wang and Ya-dong Yang, Eur. Phys. J. C **34** 291-296 (2004).

[9] X. Li *et al*, Eur. Phys. J. C**36**, 97 (2004).

[10] J. Eeq *et al*, Eur. Phys. J. C**42**, 29 (2005).

[11] Y. Li *et al.*, [arXiv:hep-ph/0308243], J. Phys. G **31** : 2005.

[12] A. Zupanc *et al*, Belle Collaboration, PRD **75**, 091102 (2007).

[13] W.M.Yao *et al*, 2006 J.Phys.G: Nucl.Part.Phys.33 1.

[14] C. H. Chen *et al*, Eur. Phys. J. C**46**, 367 (2006).

[15] M. Gronau and J. L. Rosner, [arXiv:hep-ph/0805.4601], published in Phys. Rev. D **78**, 033011 (2008).

[16] B. Blok, M. Gronau and J. L. Rosner, Phys. Rev. Lett **78** (1997) 3999.

[17] M. Benayoun *et al.*, Phys. Rev. D **59** (1999) 114027.

[18] M. Benayoun *et al.*, Eur. Phys. J. C **55** (2008) 199.

[19] M. Gronau and J. L. Rosner, [arXiv:hep-ph/0806.3584], published in Phys. Lett. B **666**, 185 (2008).

[20] B. Aubert *et al.*, *BABAR* Collaboration, Phys. Rev. D **76** (2007) 031101.

[21] B.Aubert *et al*, *BABAR* Collaboration, Phys.Rev.Lett **91**, 071801 (2003).

[22] S. Kurokawa and E. Kikutani *et al.*, Nucl. Instrum. Methods Phys. Res. Sect. A **499**, 1 (2003).

[23] A. Abashian *et al.*, Belle Collaboration, Nucl. Instrum. Methods Phys. Res. Sect. A **479**, 117 (2002).

[24] G. Alimonti *et al.*, Nucl. Instrum. Methods Phys. Res. Sect. A **453**, 71 (2000).

[25] Y.Ushiroda, Nucl. Instrum. Methods Phys. Res. Sect. A **511**, 6 (2003).

[26] H. Hirano *et al.*, Nucl. Instrum. Methods Phys. Res. Sect. A **455**, 294 (2000).

[27] T. Iijima *et al.*, Nucl. Instrum. Methods Phys. Res. Sect. A **453**, 321 (2000).

[28] I. Adachi *et al.*, Nucl. Instrum. Methods Phys. Res. Sect. A **355**, 390 (1995).

[29] H. Kichimi *et al.*, Nucl. Instrum. Methods Phys. Res. Sect. A **453**, 315 (2000).

[30] K. Miyabayashi, Nucl. Instrum. Methods Phys. Res. Sect. A **494**, 298 (2002).

[31] Y. Makita *et. al.*, Adv. Cryog. Eng. **37**, 401 (1992); Adv. Cryog. Eng. **43A**, 221 (1998).

[32] A. Abashian *et al.*, Nucl. Instrum. Methods Phys. Res. Sect. A **491**, 69 (2002).

[33] Y. Ushiroda *et al.*, Nucl. Instrum. Methods Phys. Res. Sect. A **438**, 460 (1999).

[34] K. Hanagaki *et al.*, Nucl. Instrum. Methods Phys. Res. Sect. A **485**, 490 (2002).

[35] A. Abashian *et al.*, Nucl. Instrum. Methods Phys. Res. Sect. A **491**, 69 (2002).

[36] B. Casey, Belle Note 296 and 390.

[37] EvtGen B meson decay generator developed by CLEO and Babar Collaboration, see at "http://www.slac.stanford.edu/ lange/EvtGen/".

[38] D. J. Lange, Nucl. Instr. and Meth. **A462**, 152(2001).

[39] GEANT detector Description and Simulation Tool, CERN Program Library Long Writeup W5013 (1993); R. Brun *et al.*, CERN Report DD/EE/84-1, (1984).

[40] B.Aubert *et al*, *BABAR* Collaboration, Phys. Rev. D **65**, 32001 (2002).

[41] G. C. Fox and S. Wolfram, Phys. Rev. Lett. **41**, 1581 (1978).

[42] Belle Collaboration, Tracking group webpage, see at "http://belle.kek.jp/ hitoshi/private/track/error/index.html".

[43] Belle Collaboration, KID group webpage, see at "http://belle.kek.jp/group/pid_joint/".

[44] S.Nishida, Belle Note 779.

[45] M.C.Chang, Belle Note 884, p26; Belle Collaboration, Lepton-ID group webpage, see at "http://belle.kek.jp/group/pid_joint/".

[46] M. Gronau and J. L. Rosner, [arXiv:hep-ph/0808.3761].

[47] B. Aubert *et al.*, *BABAR* Collaboration, Phys. Rev. D **76**, 051103 (2007).

[48] B. Aubert *et al.*, *BABAR* Collaboration, Phys. Rev. D **74**, 011102 (2006).

[49] T. Bergfeld *et al.*, CLEO Collaboration, Phys. Rev. Lett **81**, 272 (1998).